

Black Hole Spectroscopy and Tests of General Relativity with GW250114

(The LIGO Scientific Collaboration, the Virgo Collaboration, and the KAGRA Collaboration)*

(Dated: September 11, 2025)

The binary black hole signal GW250114, the loudest gravitational wave detected to date, offers a unique opportunity to test Einstein’s general relativity (GR) in the high-velocity, strong-gravity regime and probe whether the remnant conforms to the Kerr metric. Upon perturbation, black holes emit a spectrum of damped sinusoids with specific, complex frequencies. Our analysis of the post-merger signal shows that at least two quasi-normal modes are required to explain the data, with the most damped remaining statistically significant for about one cycle. We probe the remnant’s Kerr nature by constraining the spectroscopic pattern of the dominant quadrupolar ($\ell = m = 2$) mode and its first overtone to match the Kerr prediction to tens of percent at multiple post-peak times. The measured mode amplitudes and phases agree with a numerical-relativity simulation having parameters close to GW250114. By fitting a parameterized waveform that incorporates the full inspiral–merger–ringdown sequence, we constrain the fundamental ($\ell = m = 4$) mode to tens of percent and bound the quadrupolar frequency to within a few percent of the GR prediction. We perform a suite of tests—spanning inspiral, merger, and ringdown—finding constraints that are comparable to, and in some cases 2–3 times more stringent than those obtained by combining dozens of events in the fourth Gravitational-Wave Transient Catalog. These results constitute the most stringent single-event verification of GR and the Kerr nature of black holes to date, and outline the power of black-hole spectroscopy for future gravitational-wave observations.

Introduction— On January 14, 2025, the LIGO detectors [1] recorded the loudest gravitational-wave (GW) signal to date, GW250114_082203 (hereafter GW250114) [2]. The Virgo [3] and KAGRA [4] interferometers were offline at the time. The high network signal-to-noise ratio (SNR) of 76 makes GW250114 an especially powerful probe of whether Einstein’s theory of general relativity (GR) [5], and, in particular, its rotating black hole (BH) solution [6], accurately describe the observed gravitational radiation.

The non-linearity of Einstein’s field equations, coupled with the interdependence of metric and matter, the inherent gauge freedom, and the complexity of the initial-value problem [7, 8] have made solving these equations notoriously challenging. Following the spherically symmetric solution [9] in 1916, the search for an exact rotating axisymmetric solution in vacuum spanned nearly 50 years, until the Kerr metric breakthrough [6]. This was followed by efforts to establish the uniqueness of static and stationary solutions, including their full characterization by conserved quantities, such as mass, spin, and charge [10–15]. The Kerr metric’s simplicity has enabled the derivation of unexpected properties, including integrability for geodesic motion [16], the Penrose process [17, 18], and the four laws of BH mechanics [19]. The solution’s application to rotating BHs has had a profound impact on astrophysics, particularly once quasars were discovered [20]. The Kerr solution underpins waveform models used to detect GWs and infer properties of dark objects. Thus, finding that these objects do not conform to Kerr BHs would have far-reaching implications for both astrophysics and fundamental physics.

From shortly after its inception, the theory of GR has withstood a broad array of experimental probes. Nevertheless, there are open questions associated to BHs, such as their stability [21–24], the existence of singularities inside their event horizon [25], and Hawking’s information-loss paradox [26, 27]. Furthermore, GR is known to be incomplete in the quantum domain and requires a dark sector (dark matter

and dark energy) to explain cosmological observations, motivating continued searches for possible deviations and viable extensions of the theory [28]. Some gravity theories alternative to GR admit the Kerr metric as a solution [29, 30], thus tests of GR and tests of Kerr spacetime are complementary.

In the last ten years, GW observations from binary black hole (BBH) coalescences [31, 32] (as well as, from binary neutron stars and mixed binaries) have provided a unique laboratory for testing GR in the strong-gravity, dynamical and high-velocity regime, where potential departures from GR are expected to be most pronounced [28–30, 33]. Since the first detection of a BBH coalescence [34, 35], the growing catalog of GW events [32, 36–39] has enabled increasingly stringent bounds of the inspiral, merger, and ringdown phases [40–43]. These results complement other GR investigations—Solar System tests, binary-pulsar experiments, observations of massive BHs at galactic centers, and cosmological measurements [28, 44–49]—which span low-velocity, quasi-static, weak-field regimes and, in some cases, strong-field environments with self-gravitating bodies.

In vacuum, BHs in binaries adiabatically and steadily approach each other during the inspiral until they merge, driven by GW emission, a purely tensorial radiation in GR, dominated by the quadrupolar multipole [50]. According to GR, after the two BHs merge, a highly distorted remnant BH is formed, which equilibrates by emitting gravitational radiation [51–53]. In the 1970s, Vishveshwara and Press [54, 55], using results from Regge, Wheeler, and Zerilli [56, 57], made a significant discovery. In response to an incoming pulse of radiation, BHs ring the spacetime, emitting a superposition of damped sinusoids with discrete frequencies and decay times, depending solely on the intrinsic properties of the BH, notably its mass and spin. This follows from the no-hair theorem [6, 10–15], which states that in four-dimensional vacuum GR, a stationary BH that is non-singular outside the horizon is fully characterized by its mass and spin. Since those pioneering works [54, 55], using sophisticated analytical and nu-

merical methods in BH perturbation theory [58–62], the full first-order BH spectrum has been computed for rotating BHs, revealing also the presence of GW tails [63, 64] at late times. It was also noted [61] that with the advent of GW astronomy, detecting BH’s quasi-normal mode (QNM) frequencies could confirm their existence with a certainty comparable to the way the 21 cm line unequivocally identifies interstellar hydrogen. This started the BH-spectroscopy program [61, 65–71]. A measurement of the frequency and damping rate of a single mode suffices to constrain the final-state mass and spin. Measurements of multiple mode frequencies and damping times enable a test of the no-hair theorem [17, 72–74] through the consistency of the modes’ properties with the Kerr prediction [6]. In principle, the QNMs are affected by electromagnetic charges, but we expect the latter to be negligible for astrophysical BHs [75–78]. Several studies in the last few years have investigated the presence of QNMs in GW data claiming different levels of significance [35, 43, 79–84].

In this *Letter*, we perform several studies of GW250114, aimed at constraining deviations from the GR predictions throughout the inspiral, merger and ringdown; the Kerr nature of the components in the binary, and of the remnant via BH spectroscopy. Extending the recent work in Abac *et al.* [2], we investigate the post-merger stage with different ringdown models and methods. We corroborate our findings for the amplitudes and phases of the quadrupolar QNMs with results of a numerical-relativity (NR) simulation having parameters close to GW250114. We bound the spectroscopic pattern of the dominant quadrupolar mode and its first overtone to match the Kerr prediction at multiple post-peak times, while constraining, for the first time, the hexadecapolar fundamental-mode frequency. We set the most stringent bounds on the post-Newtonian (PN) parameters determining the GW phasing during the inspiral, perform signal consistency tests and use them to assess the increase of the BHs area from the inspiral to the ringdown at high credibility. Overall, GR and the Kerr metric once again remain empirically unshaken.

GW250114— Using the inspiral–merger–ringdown (IMR) quasi-circular, spin-precessing `NRSur7dq4` model [85], Abac *et al.* [2] found that the wave morphology is consistent with a BBH with component masses $33.6_{-0.8}^{+1.2} M_{\odot}$ and $32.2_{-1.3}^{+0.8} M_{\odot}$ and dimensionless spin magnitudes ≤ 0.24 and ≤ 0.26 (90% credible intervals). Its eccentricity is constrained to $e \leq 0.03$ at a reference frequency of 13.33 Hz, using eccentric aligned-spin models [86, 87].

BH spectroscopy of the remnant alone— In GR, after a dynamical phase surrounding a BBH merger, the post-merger signal is dominated by a superposition of exponentially damped sinusoids corresponding to QNMs of the final Kerr remnant with redshifted mass $M_f(1+z)$, where z is the cosmological redshift, and dimensionless spin χ_f [51–53].

While the prompt response [65, 88, 89], dynamical effects [90–92], higher-order perturbative terms [93–96], and nonlinearities [51] are expected to contribute to the early post-merger signal, they are subdominant to the QNMs at sufficiently late times [97, 98]. Gravitational-wave tails [63, 64,

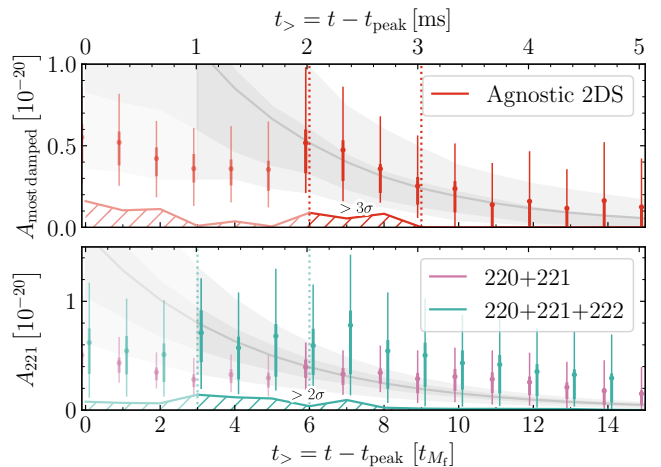


FIG. 1. Consistency of post-merger data with two QNMs. *Top:* The inferred amplitude of the most rapidly decaying damped sinusoid for the 2DS model at different fit times as measured by `ringdown`. The dots indicate posterior medians, while the thick (thin) bars indicate the 50% (90%) credible interval; for each time, they have been offset slightly for clarity. The gray bands predict the median, 50%, and 90% credible ranges of amplitudes over time from the $t_{>} = 6t_{M_f}$ fit, marked by the first dotted line. The second dotted line at $t_{>} = 9t_{M_f}$ indicates the latest time that the 90% credible range of the amplitude is distinct from zero. The hatched region shows the greater than 3σ -equivalent credible region for the amplitude being strictly positive. *Bottom:* The inferred amplitude of the 221 mode for the 220+221 (pink) and 220+221+222 (green) models as measured by `pyRing`. The first dotted line indicates $t_{>} = 3t_{M_f}$, beyond which 220+221+222 fits yield 221 amplitudes consistent with that at $t_{>} = 6t_{M_f}$. The second dotted line indicates $t_{>} = 6t_{M_f}$. The hatched curve shows the $> 2\sigma$ -equivalent credible region.

99–102] dominate at much later times. Here, because of theoretical modeling uncertainties, we neglect these other contributions, focusing on the exponentially decaying sinusoidal QNM component and assume that the plus and cross polarizations of the post-merger signal at the detectors take the form [35, 68]

$$h_+ - i h_{\times} = \sum_{\substack{\ell \geq 2 \\ 0 \leq m \leq \ell}} e^{-t/\tau_{\ell m n}} (A_{\ell m n}^R e^{-2\pi i f_{\ell m n} t} + A_{\ell m n}^L e^{2\pi i f_{\ell m n} t}), \quad (1)$$

where the complex numbers $A_{\ell m n}^R$ and $A_{\ell m n}^L$ encode the amplitudes and phases of the right- and left-circularly polarized components of the mode, and depend on the excitations imprinted on the spacetime by the progenitors’ dynamics [103–108]. The frequency $f_{\ell m n}$ and the damping time $\tau_{\ell m n}$ correspond to the Kerr QNM frequencies and damping times, and are indexed by the angular-mode numbers ℓ and m , and the radial-overtone number n [58–60]. The amplitude of the elliptically polarized mode at time $t = 0$, which we take to be the starting time of fits of Eq. (1) to GW250114, is $A_{\ell m n} = |A_{\ell m n}^R| + |A_{\ell m n}^L|$ [109]. Given GW250114’s properties, in Eq. (1) we have neglected retrograde modes, which are known to be less excited and less important than prograde modes for

this type of system [105, 110, 111].

We employ `ringdown` [80, 109] and `pyRing` [79, 112] to fit Kerr models of the form Eq. (1), as well as models with agnostic complex frequencies, to the post-peak signal from GW250114, starting at a range of times, $t_>$, after t_{peak} : the time at which NRSur7dq4's maximum likelihood strain magnitude over the two-sphere achieves its maximum [2, 79, 80, 85, 109, 113]. We adopt the reference peak time, mass, and sky location from the ringdown fits in Abac *et al.* [2], with $t_{M_f} = (1+z)GM_f/c^3 = 0.337$ ms. Henceforth, we refer to the Kerr modes in Eq. (1) as ℓmn , and a sum of multiple modes is denoted as $\ell mn + \ell' m' n'$. The `ringdown` and `pyRing` codes have different native priors and run settings, and therefore produce results for this analysis that differ [2]. The results from both codes are sufficiently qualitatively similar, however, that in most cases we show results from only one or the other code throughout.

As shown in Abac *et al.* [2], the post-peak data of GW250114 is consistent with the 220 and 221 QNMs. Here, we further motivate this identification, extend this study using other ringdown models and methods, and test the remnant's Kerr nature at different post-peak times. In the Supplemental Material, we also validate the use of Eq. (1) at the times at which we apply our QNM models by comparing to NR waveforms. We start by adopting an agnostic sum of two damped sinusoids (2DS) whose complex amplitudes, frequencies, and damping times are arbitrary [35, 42, 43]. In the top panel of Fig. 1, we show that the amplitude of the more rapidly decaying damped sinusoid at various fit start times $t_>$ is bounded away from zero at $> 3\sigma$ until $t_> > 9t_{M_f}$, and it is non-zero at 3.5σ at $t_> = 6t_{M_f}$. By examining the frequencies and damping times of the two damped sinusoids shown by the red contours in Fig. 2 (the other contours will be discussed later), we find that they are broadly consistent with the 220 and 221 QNMs predicted from the remnant mass and spin inferred from the IMR analysis of GW250114 in GR. This motivates fitting GW250114 with the 220+221 model. In the bottom panel of Fig. 1, which shows the amplitude of the 221 QNM at various fit start times, we see that for the 220+221 model the 221 QNM's amplitude is not only bounded away from zero, but is consistent with the exponential decay expected within the error bounds of the 221 QNM fit at $t_> = 6t_{M_f}$ for $t_> \geq 6t_{M_f}$. At earlier times, the amplitude deviates from its expected value, suggesting a breakdown of the 220+221 model. Motivated by analysis of NR simulations [114], we find that if the 222 QNM is added to the fit, then consistency at the 90% level with the amplitude at $t_> = 6t_{M_f}$ is obtained until $t_> \geq 3t_{M_f}$, even though the amplitude of the 222 QNM is never confidently measured away from zero in these fits. These findings suggest that the data is indeed consistent with the 220 and 221 QNMs over a range of times.

In the Supplemental Material, we corroborate these results using a NR simulation in GR. Specifically, we demonstrate that the results in Fig. 1 are broadly consistent with that of a simulated signal of a NR simulation with parameters close to GW250114; we show that the relative amplitudes

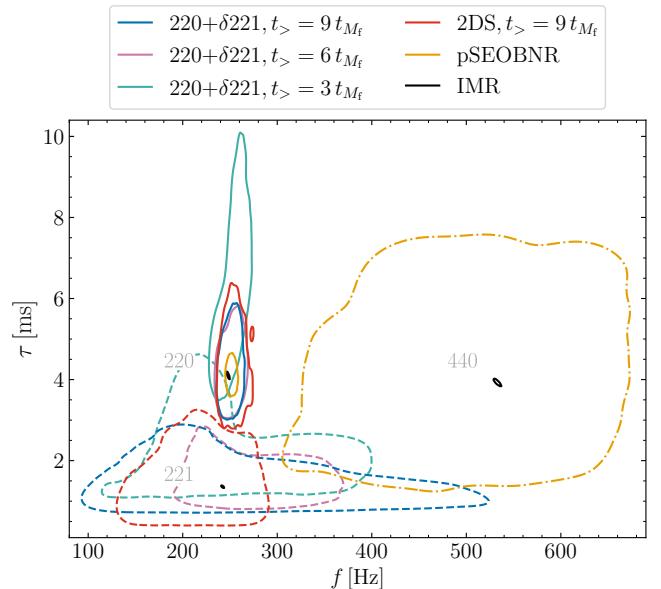


FIG. 2. BH spectroscopy with different QNMs. The 90% credible regions for the 220 (solid) and 221 (dashed) QNM frequencies and damping times as measured when fitting the 220+ δ 221 model at $t_> \in \{3, 6, 9\}t_{M_f}$ (green, pink, blue) and the 2DS model at $t_> = 9t_{M_f}$ (red). In orange, the constraints from the pSEOBNR analysis for the 220 (solid) and 440 (dot-dashed) QNMs. Black curves indicate the 220, 221, and 440 frequencies and damping times inferred from the IMR remnant mass and spin posteriors.

and phases of GW250114's 220 and 221 QNMs are consistent with those of the NR simulation at the $\geq 38\%$ credible level for $t_> \in [3, 9]t_{M_f}$. Separately, using GW250114 we also find consistency among the final mass and spin computed with the IMR analysis and the various QNM models we fit.

In Fig. 2, we probe the Kerr nature of the remnant. We examine the fit to the post-peak data of GW250114 with a 220+ δ 221 model whose 221 QNM's frequency and damping time (f_{221} and τ_{221}) are allowed to vary from their Kerr values ($f_{221,\text{Kerr}}$ and $\tau_{221,\text{Kerr}}$) by $\delta\hat{f}_{221} = \ln(f_{221}/f_{221,\text{Kerr}})$ and $\delta\hat{\tau}_{221} = \ln(\tau_{221}/\tau_{221,\text{Kerr}})$. As suggested by the 2DS fit, the data are particularly consistent with the 220 and 221 QNMs predicted by the remnant mass and spin inferred by the full IMR analysis. More specifically, we constrain $\delta\hat{f}_{221} = -0.13^{+0.61}_{-0.16}$ at $t_> = 3t_{M_f}$, $\delta\hat{f}_{221} = 0.09^{+0.29}_{-0.30}$ [2] at $t_> = 6t_{M_f}$, and $\delta\hat{f}_{221} = -0.07^{+0.72}_{-0.53}$ at $t_> = 9t_{M_f}$, all at the 90% credible level. However, the recovered amplitude of the 221 QNM is not consistent with values at later times in the $3t_{M_f}$ fit, indicating that the model may be fitting other content at these times. Previously, analysis using the third Gravitational-Wave Transient Catalog (GWTC-3.0) [43] set $\delta\hat{f}_{221} = 0.01^{+0.27}_{-0.28}$ by analyzing the data from the peak onward using `pyRing`, and hierarchically combining results from 21 events [115]. In the following section, we will return to this figure to discuss the pSEOBNR analysis.

Additionally, we perform an analysis that does not measure the mode amplitudes, but filters out successive Kerr QNMs

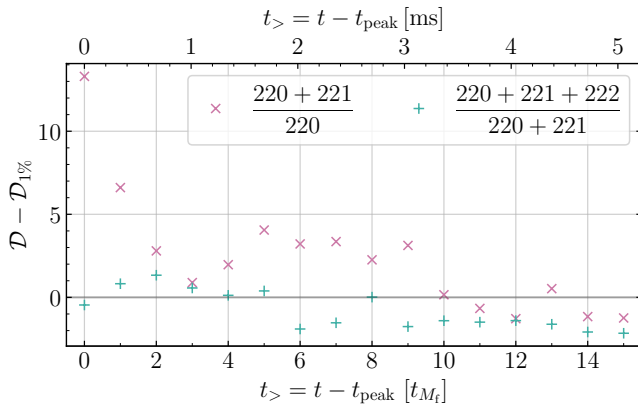


FIG. 3. Filtering out two QNMs in the post-merger data. Detection statistics for the QNMRF analysis with varying mode content relative to the 1% FAP threshold over time [119]. At times $t_> \leq 10 t_{M_f}$, the QNMRF finds strong support for the 220+221 model over the single-mode 220 model. The 220+221+222 model is weakly preferred over the 220+221 model from $t_< = 1 t_{M_f}$ to $t_< = 5 t_{M_f}$.

from the data in the frequency domain: the QNM rational filter (QNMRF) [116–118]. We adopt a hybrid Bayesian-like approach, with a detection statistic \mathcal{D} that is analogous to a logarithmic Bayes factor, yet differs from the Bayes factors used in other time-domain ringdown analyses (see details in Supplemental Material). Figure 3 shows the difference between the QNMRF detection statistic and the detection statistic corresponding to a 1% false-alarm probability (FAP) for the 220+221 and 220+221+222 models. Like the other analyses, the QNMRF finds strong support for the 220+221 model over the single-mode 220 model for times $t_> \leq 10 t_{M_f}$. Additionally, the three-mode 220+221+222 model is more weakly preferred over the 220+221 model from $t_< = 1 t_{M_f}$ to $t_< = 5 t_{M_f}$. This provides independent evidence that GW250114 is consistent with the 220 and 221 QNMs.

BH spectroscopy with full signal— So far, we have treated the complex amplitudes of the QNMs in Eq. (1) as free parameters, and directly constrained them from the data using only the post-peak signal. When these amplitudes are instead predicted from the binary’s properties using NR simulations in GR, consistency tests are feasible even with a single mode [43, 84, 120]. This results in a more stringent test of GR, at the cost of stronger assumptions about the emission process: most existing amplitude models assume the perturbed BH originates from a binary merger, and are restricted to quasi-circular orbits [103–108].

Including additional pre-merger information, one can test for deviations in QNM frequencies by analyzing a full IMR waveform calibrated to NR simulations. The pSEOBNR analysis [120–123] introduces fractional deviations ($\delta\hat{f}_{\ell m 0}$, $\delta\hat{\tau}_{\ell m 0}$) to the frequency and decay time of the fundamental QNMs in the ringdown description of SEOBNRv5PHM [124, 125] as:

$$f_{\ell m 0} = f_{\ell m 0}^{\text{GR}} (1 + \delta\hat{f}_{\ell m 0}), \quad \tau_{\ell m 0} = \tau_{\ell m 0}^{\text{GR}} (1 + \delta\hat{\tau}_{\ell m 0}). \quad (2)$$

The GR predictions for these quantities are obtained us-

ing the final mass and spin of the remnant BH, estimated using NR fits based on the measured component masses and spins [126, 127]. Rather than isolating the post-merger stage, excluding the inspiral and merger phases, the analysis uses the full IMR signal, assuming GR holds up to the merger. The merger–ringdown model is based on a factorized ansatz: the contributions of the fundamental QNMs, modified via the parametrization in Eq. (2), are multiplied by phenomenological, time-dependent amplitudes calibrated to NR [125, 128, 129]. These amplitudes aim to capture the ringdown prompt response [65, 88, 89] and dynamical phase [90–92]. As for now, this approach enables constraints on fundamental QNMs, but not on overtones, whose effects are implicitly absorbed by the time-dependent amplitudes rather than being parameterized explicitly.

We first perform an analysis allowing for deviations in the dominant 220 QNM only, which has been the focus of previous constraints [42, 43, 121, 123]. Owing to GW250114’s high SNR (~ 65 up to merger and ~ 40 post-merger), we also extend the analysis to probe higher fundamental QNMs. The nearly equal masses and low spins of the binary’s components imply that multipoles with odd m are suppressed due to rotational symmetry, while even- m multipoles are expected to be more prominent [98, 130, 131]. The inclination ($\Theta = 0.78^{+0.19}_{-0.23}$ rad [2] at a reference frequency of 20 Hz, when folded to $[0, \pi/2]$) and azimuthal phase inferred from GW250114 favor the excitation of the $(\ell, |m|) = (4, 4)$ multipoles [2], which contribute an SNR of $3.6^{+1.4}_{-1.5}$ to the full IMR signal [132]. Therefore, we perform an analysis including deviations in both the 220 and 440 QNMs. We find minimal correlation between the deviation parameters of the two modes, and in the following we report constraints on $(\delta\hat{f}_{220}, \delta\hat{\tau}_{220})$ from the joint fit.

The results are summarized in Fig. 4. The frequencies and damping times of both modes are consistent with the predictions of GR, based on the Kerr remnant parameters inferred from the inspiral. The dominant 220 QNM is especially well constrained, with $\delta\hat{f}_{220} = 0.02^{+0.02}_{-0.02}$ and $\delta\hat{\tau}_{220} = -0.01^{+0.10}_{-0.09}$. Owing to the exceptional SNR of this signal, these constraints are roughly twice as stringent as those obtained by hierarchically combining [115, 133] results from 17 events in the fourth Gravitational-Wave Transient Catalog (GWTC-4.0) [134], which have SNR above 8 in the inspiral and post-inspiral stages. That analysis yielded $\delta\hat{f}_{220} = 0.00^{+0.06}_{-0.06}$ and $\delta\hat{\tau}_{220} = 0.16^{+0.18}_{-0.16}$. A measure of consistency with GR is provided by the GR quantile Q_{GR} [42], which corresponds to the cumulative posterior probability enclosed by the isoprobability surface passing through the GR prediction. A lower (higher) value of Q_{GR} indicates better (worse) consistency with GR. For GW250114, the GR quantile is 54.2%, lower than for the combined constraints from GWTC-4.0 [134], 85.1%. The GWTC-4.0 results show a mild tension with GR [134], potentially due to non-Gaussian or non-stationary noise [42, 123], parameter correlations amplified by unrealistic astrophysical priors [43, 135], intrinsic variance due to the limited number of events in the catalog [136], or unmodeled selection effects that could systematically influence which sig-

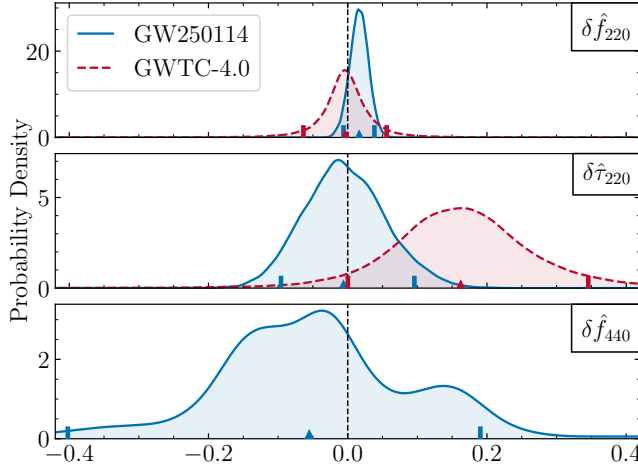


FIG. 4. Constraining the 220 and 440 QNMs using the full signal. Marginalized posterior distributions for fractional deviations in the frequency and damping time of the 220 QNM ($\delta\hat{f}_{220}$, $\delta\hat{\tau}_{220}$), and in the frequency of the 440 QNM ($\delta\hat{f}_{440}$), from the pSEOBNR analysis of GW250114. Hierarchically combined results from GWTC-4.0 [134] are also shown. Triangles mark the median values and vertical bars the symmetric 90% credible interval.

nals are included in the analysis.

We also constrain, for the first time, the frequency of the subdominant 440 QNM, obtaining $\delta\hat{f}_{440} = -0.06^{+0.25}_{-0.35}$. The damping time remains weakly constrained, with $\delta\hat{\tau}_{440} = 0.20^{+0.53}_{-0.69}$. Since the pSEOBNR method employs the entire IMR signal, it enforces continuity across the waveform and does not allow the mode amplitudes to vanish. As a result, the analysis cannot by itself establish whether the 440 QNM is present in the data. However, similar constraints do not appear in simulated signals that exclude this mode or in lower-SNR events (see details in the Supplemental Material), lending support to the interpretation that the constraint is driven by the presence of the 440 QNM in the ringdown signal of GW250114.

Beyond testing whether each mode is individually consistent with GR, one can also test whether both are consistent with originating from the same Kerr remnant, as in classical no-hair-theorem tests [61, 65–69]. In the pSEOBNR framework, this is done by reconstructing the complex frequencies of the two modes from Eq. (2), giving $f_{220} = 251.7^{+5.1}_{-5.0}$ Hz, $\tau_{220} = 4.09^{+0.42}_{-0.38}$ ms, $f_{440} = 503^{+130}_{-185}$ Hz, and $\tau_{440} = 4.7^{+2.1}_{-2.7}$ ms. Their 90% credible regions are shown as the orange solid and dot-dashed curves in Fig. 2. These are then inverted to obtain two separate estimates of the remnant’s mass and spin using fitting formulas [68], shown in Fig. 9. We find that the estimates are mutually consistent, and agree with both the IMR-inferred values and with results from ringdown remnant-alone analyses.

The presence of the (4, 4) multipole is independently supported by isolating the post-peak data in time domain, with the KerrPostmerger model in pyRing [84]. This model has also amplitudes calibrated to NR simulations at merger [129, 137,

138]. Including the (4, 4) mode is mildly favored by a \log_{10} Bayes factor of $0.54^{+0.18}_{-0.18}$ compared to a model with only the dominant (2, 2) mode. Allowing for deviations from GR with the parametrization in Eq. (2), we constrain the 220 QNM as $\delta\hat{f}_{220} = 0.09^{+0.34}_{-0.22}$ and $\delta\hat{\tau}_{220} = -0.14^{+0.25}_{-0.23}$, while the 440 mode remains unconstrained. While less stringent than pSEOBNR, this analysis quantifies the constraints achievable when isolating the remnant’s relaxation.

The stringent pSEOBNR results can improve current constraints on gravity theories beyond GR [139–143], and constrain properties of exotic compact objects [144, 145]. As a concrete example, we consider dynamical Chern-Simons (dCS) gravity [146], a parity-violating extension of GR in which the QNM spectrum receives corrections controlled by a coupling length $\sqrt{\alpha_{\text{dCS}}}$ [147]. Mapping the bound on the 220 QNM frequency to the predicted dCS correction yields an approximate constraint on the dCS coupling length of $\sqrt{\alpha_{\text{dCS}}} < 32.2$ (40.1) km, assuming purely axial (polar) perturbations [147] (using the conventions therein). These single-event bounds are competitive with recent ringdown-only analyses of GW150914, GW190521_074359, and GW200129_065458 [143]. The estimate is based on the posteriors for $\delta\hat{f}_{220}$ and remnant mass and spin from the pSEOBNR analysis, reweighted to a prior uniform in the dCS coupling length. More robust constraints could be obtained from a Bayesian analysis that directly uses waveform predictions in dCS gravity [141, 143].

Bounding post-Newtonian inspiral parameters—The inspiral regime can be treated perturbatively within the PN framework [148], an expansion in powers of v/c where the n PN order corresponds to $O([v/c]^{2n})$. As the intrinsic parameters of the binary uniquely determine the PN coefficients φ_i in the GW phase at each order, we can construct a consistency test of GR by introducing deformation parameters at each PN order [149–155]. We only consider variations in the individual PN coefficients independently, treating them as free coefficients that constrain the degree to which deviations from GR agree with the data. The inspiral deviations are constructed so as to represent a shift to the non-spinning PN coefficient, i.e., $\varphi_i \rightarrow (1 + \delta\hat{\varphi}_i)\varphi_i^{\text{NS}} + \varphi_i^{\text{S}}$, where φ_i^{NS} denotes the non-spinning coefficient and φ_i^{S} is the spin-dependent part of the PN coefficient. In GR, the coefficients at -1PN and 0.5PN are explicitly zero and should be interpreted as absolute deviations, while the other coefficients are expressed as fractional deviations.

As in the GWTC-4.0 analysis [134], we use two independent pipelines: Flexible Theory Independent (FTI) [40, 156] and Test Infrastructure for GEneral Relativity (TIGER) [157–159]. The pipelines have several methodological differences, including the cut-off frequency at which corrections are turned off and choice of waveform models used. The FTI pipeline employs the SEOBNRv5HM_ROM model [125], which is restricted to aligned-spin configurations, whereas TIGER utilizes the precessing-spin waveform model IMRPhenomXPHM_SpinTaylor [160, 161]. Due to technical changes in the pipelines, only events first reported

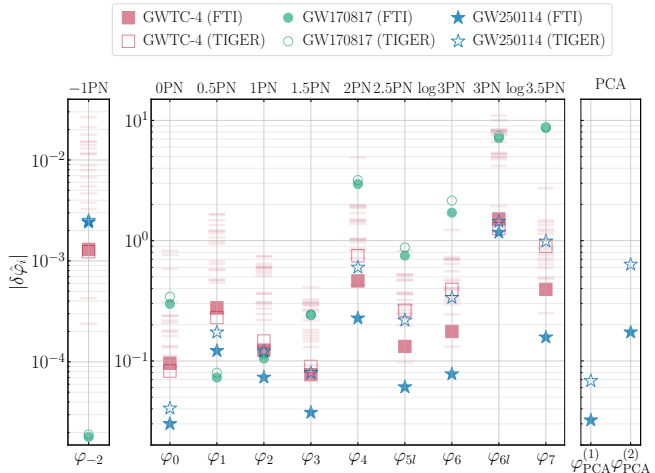


FIG. 5. Constraints on the inspiral phase from GW250114. The 90% upper bounds on the magnitude $|\delta\hat{\varphi}_i|$ of the PN inspiral deviation coefficients from -1PN to 3.5PN and the first two leading PCA parameters. For GW250114, blue filled (unfilled) stars are for FTI (TIGER). The horizontal red stripes mark the results from individual events from GWTC-4.0 using FTI. Bounds obtained by hierarchically combining the results from GWTC-4.0 are shown in the filled (unfilled) red squares for FTI (TIGER) [134]. The right panel shows constraints on the two leading PCA parameters that capture the dominant modes of deviation across the $1.5\text{--}3.5$ PN parameter space.

in GWTC-4.0 that meet the FTI or TIGER selection criteria are analyzed [134]. For FTI, we use 18 events and for TIGER, we use 24 events.

The results are summarized in Fig. 5. Due to the significantly higher SNR of GW250114 during the inspiral phase compared to the rest of the observed BBH population, the FTI analysis of GW250114 provides constraints on a subset of deviations that are 2–3 times more stringent than the joint constraints derived from a hierarchical analysis [115, 133] of the GWTC-4.0 results [134]. The bounding fractional deviations to the leading-order PN and 1.5PN coefficients are $\delta\hat{\varphi}_0 = 0.00^{+0.03}_{-0.03}$ and $\delta\hat{\varphi}_3 = -0.01^{+0.03}_{-0.02}$ for GW250114 compared to $\delta\hat{\varphi}_0 = -0.00^{+0.09}_{-0.09}$ and $\delta\hat{\varphi}_3 = 0.00^{+0.07}_{-0.07}$ for GWTC-4.0. GW250114 being a shorter signal, we do not place competitive constraints on the dipole φ_{-2} compared to those obtained from GW170817 [40]. Overall, the TIGER pipeline yields constraints that are less stringent than the combined GWTC-4.0 results [134], likely due to the differing treatment of the cutoff frequency and transition to merger–ringdown between the pipelines [134], and the inclusion of spin-precession in the TIGER analysis.

To address the limitation of varying individual PN coefficients independently, we perform a Principal-Component Analysis (PCA) to probe correlated deviations across multiple PN orders [162–165], focusing on the 1.5 to 3PN coefficients [164, 165].

The PCA analysis identifies the principal directions of parameter covariance, with the leading component corresponding to the linear combination of PN coefficients that is best

constrained by the data. The leading PCA component can therefore yield tighter bounds than the individual PN coefficients, while the sub-leading component, being orthogonal to this optimal direction, can have weaker constraints than the best measured PN coefficients. We find that the FTI pipeline constrains the leading PCA component to $\delta\hat{\varphi}_{\text{PCA}}^{(1)} = -0.01^{+0.02}_{-0.02}$ (slightly better constrained than $\delta\hat{\varphi}_3 = -0.01^{+0.03}_{-0.02}$) and the sub-leading component to $\delta\hat{\varphi}_{\text{PCA}}^{(2)} = 0.04^{+0.13}_{-0.13}$, consistent with GR (see Fig. 5). A comparison of the PCA results to GWTC-4.0 is technically challenging as the PCA components correspond to different linear combinations of PN parameters for each event. This means that hierarchical inference requires modelling the joint distribution across all six PN coefficients [165]. Further details are presented in the Supplemental Material.

Signal consistency tests— We now construct an analysis complementary to the other tests, focusing on the consistency between different portions of the signal, by employing dimensionless deviation parameters that quantify the fractional difference between the remnant mass M_f and spin χ_f inferred from the low- ($f < f_c^{\text{IMR}}$) and high-frequency ($f > f_c^{\text{IMR}}$) portions of the GW signal [166–168]. The cutoff f_c^{IMR} is taken to be the GW frequency of the $(2, 2)$ -mode at the innermost circular orbit of the remnant Kerr BH [169]. The remnant properties are calculated using NR-calibrated fits for the final-state [127, 170, 171] applied to the median values of the redshifted component masses, spin magnitudes, and spin angles as inferred from the full IMR analysis [41–43]. Inference is performed in each of the frequency regimes using `IMRPhenomXPHM.SpinTaylor` [160, 161], with priors that are uniform in component mass and spin magnitude, and isotropic in the spin orientation. This choice of priors leads to highly non-uniform priors on the deviation parameters, and we therefore reweight the posteriors to impose uniform priors on them [42, 43].

If GR is valid, and our waveform models are sufficiently accurate, the analysis in each of these regimes should yield consistent results. Thus, we have $\Delta M_f/\bar{M}_f = 2(M_f^{\text{insp}} - M_f^{\text{postinsp}})/(M_f^{\text{insp}} + M_f^{\text{postinsp}})$, and $\Delta\chi_f/\bar{\chi}_f = 2(\chi_f^{\text{insp}} - \chi_f^{\text{postinsp}})/(\chi_f^{\text{insp}} + \chi_f^{\text{postinsp}})$, such that the GR limit is given by $\Delta M_f/\bar{M}_f = \Delta\chi_f/\bar{\chi}_f = 0$. The core results are summarized in Fig. 6. We infer $\Delta M_f/\bar{M}_f = 0.02^{+0.07}_{-0.06}$ and $\Delta\chi_f/\bar{\chi}_f = -0.01^{+0.11}_{-0.11}$ from GW250114. We compare these results with the ones obtained by hierarchically combining 30 events, of which 12 are first reported in GWTC-4.0 [134], which yields $\Delta M_f/\bar{M}_f = 0.01^{+0.07}_{-0.06}$ and $\Delta\chi_f/\bar{\chi}_f = -0.04^{+0.07}_{-0.07}$. Remarkably, the constraints derived from GW250114 alone yield a consistency test of comparable stringency to the combined analysis of GWTC-4.0 [134]. The GR quantile for the two-dimensional posteriors from GW250114 is 49.5%, compared to 51.1% for the GWTC-4.0 analysis [134].

We also exploit the results of the consistency test to determine at what statistical significance the Hawking area theorem [172], a fundamental consequence of the second law of BH mechanics, holds. This theorem states that the horizon

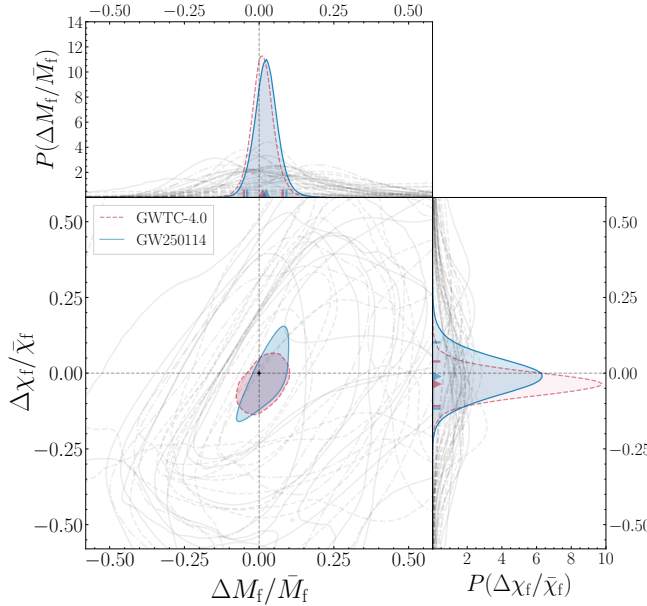


FIG. 6. Consistency of GW250114 with a BBH in GR using data from the inspiral and merger–ringdown. The 90% credible regions of the two-dimensional posteriors on $\Delta M_f / \bar{M}_f$ and $\Delta \chi_f / \bar{\chi}_f$ for GW250114 (filled blue), with $(0, 0)$ being the expected value for GR. The side panels show the marginalized posteriors. The gray two-dimensional posteriors show the results from individual events in GWTC-4.0 [134], while the red shaded posteriors denote constraints derived from a hierarchical inference on these events. Triangles mark the median values and vertical bars the symmetric 90% credible interval.

area of a BH cannot decrease over time. Our analysis yields a credibility of $4.8\sigma_{\text{IMR}}^{\text{CT}}$, representing the statistical significance in standard deviations of the difference between the mean total area of the initial BHs and the mean final-BH’s area. This test differs from the more agnostic strategy followed in Abac *et al.* [2], where the initial and final areas of the objects are computed excluding the GW data around the merger signal. In addition, the test performed here splits the data in the frequency-domain, which is not equivalent to the time-domain analysis in Abac *et al.* [2]. See the Supplemental Material for the main results in Fig. 12 and further details.

Finally, in the Supplemental Material we also report the results of a residuals test [35, 173, 174], which looks for excess coherent power in the detector network after the maximum-likelihood waveform has been subtracted from the data. The upper limit for the residual network SNR is 6.86 at 90% credibility (p -value 0.34, see Supplemental Material). Thus, we do not find any statistically significant coherent power beyond what is expected from the noise background.

Conclusion— The outstanding improvement of the LIGO detectors in the last decade [175–177] has enabled unprecedented observations [32, 178]. In particular, GW250114 was observed with the largest SNR to date (65 up to merger and 40 post-merger) [2], approximately three times that of the similar event GW150914 [179]. We have performed the most stringent

suite of tests of GR and the Kerr nature for a BBH coalescence to date. Probing the inspiral, merger and ringdown stages, we have set constraints comparable, and in some cases 2–3 times more stringent, than the ones obtained combining tens loudest events of GWTC-4.0 [134]. At least three QNMs have been identified or constrained with several methods and models: the quadrupolar 220 fundamental and first overtone 221, and the hexadecapolar 440 mode. We have found that their spectroscopic pattern [61, 65–69] aligns with the Kerr metric prediction, and their amplitudes are consistent with those measured in a NR simulation of GW250114-like systems in GR. In summary, the single, loud event GW250114 has yielded the scientific return of dozens of previous detections, offering a preview of the unprecedented science that upcoming LIGO–Virgo–KAGRA observing runs [180] will unlock.

Strain data from the LIGO detectors for GW250114 are available from the Gravitational Wave Open Science Center [181]. All the material required for reproducing the figures, including scripts and posterior distributions from the analyses, is available in the data release [182].

Acknowledgements— This work made use of the following software, listed in alphabetical order: `arviz` [183], `Asimov` [184], `astropy` [185–187], `BayesWave` [188], `Bilby` [189, 190], `Bilby_TGR` [191], `cpnest` [192], `dynesty` [193], `gwpy` [194, 195], `h5py` [196], `IMRPhenomXPHM_SpinTaylor` [160, 161], `jupyter` and `ipython` [197–199], `lalsuite` [200, 201], `matplotlib` [202, 203], `NRSur7dq4` [85], `numpy` [204], `pandas` [205, 206], `pesummary` [207], `pyRing` [79, 112], `pySEOBNR` [208], `python` [209], `qnm` [210], `ringdown` [109, 211], `scipy` [212, 213], `seaborn` [214], `SEOBNRv5PHM` and `SEOBNRv5HM_ROM` [124, 125, 215, 216], `sxs` [217], `tqdm` [218],

Late in the preparation of this manuscript, an error in the likelihood function used in the `Bilby` inference code was discovered, leading to an overly constrained likelihood [219]. The impact of this error is discussed in detail in the GWTC-4.0 methods paper [220]. Following from investigations presented therein, we expect differences in the inferred posterior distributions due to this error to be small. A full correction of the results was not possible for the current version of the manuscript. Results for `pSEOBNR`, `FTI`, and `TIGER` have been corrected. For the IMR consistency test, only events analyzed before GWTC-4.0 remain to be corrected. Updated results for `PCA` and the IMR consistency test using a corrected likelihood function will be provided in a future revision, before publication. Other analyses are unaffected by this error.

This material is based upon work supported by NSF’s LIGO Laboratory, which is a major facility fully funded by the National Science Foundation. The authors also gratefully acknowledge the support of the Science and Technology Facilities Council (STFC) of the United Kingdom, the Max-Planck-Society (MPS), and the State of Niedersachsen/Germany for support of the construction of Advanced LIGO and construction and operation of the GEO 600 detector. Additional support for Advanced LIGO was provided by the Australian Research Council. The authors gratefully acknowledge the Ital-

ian Istituto Nazionale di Fisica Nucleare (INFN), the French Centre National de la Recherche Scientifique (CNRS) and the Netherlands Organization for Scientific Research (NWO) for the construction and operation of the Virgo detector and the creation and support of the EGO consortium. The authors also gratefully acknowledge research support from these agencies as well as by the Council of Scientific and Industrial Research of India, the Department of Science and Technology, India, the Science & Engineering Research Board (SERB), India, the Ministry of Human Resource Development, India, the Spanish Agencia Estatal de Investigación (AEI), the Spanish Ministerio de Ciencia, Innovación y Universidades, the European Union NextGenerationEU/PRTR (PRTR-C17.I1), the ICSC - CentroNazionale di Ricerca in High Performance Computing, Big Data and Quantum Computing, funded by the European Union NextGenerationEU, the Comunitat Autònoma de les Illes Balears through the Conselleria d'Educació i Universitats, the Conselleria d'Innovació, Universitats, Ciència i Societat Digital de la Generalitat Valenciana and the CERCA Programme Generalitat de Catalunya, Spain, the Polish National Agency for Academic Exchange, the National Science Centre of Poland and the European Union - European Regional Development Fund; the Foundation for Polish Science (FNP), the Polish Ministry of Science and Higher Education, the Swiss National Science Foundation (SNSF), the Russian Science Foundation, the European Commission, the European Social Funds (ESF), the European Regional Development Funds (ERDF), the Royal Society, the Scottish Funding Council, the Scottish Universities Physics Alliance, the Hungarian Scientific Research Fund (OTKA), the French Lyon Institute of Origins (LIO), the Belgian Fonds de la Recherche Scientifique (FRS-FNRS), Actions de Recherche Concertées (ARC) and Fonds Wetenschappelijk Onderzoek - Vlaanderen (FWO), Belgium, the Paris Île-de-France Region, the National Research, Development and Innovation Office of Hungary (NKFIH), the National Research Foundation of Korea, the Natural Sciences and Engineering Research Council of Canada (NSERC), the Canadian Foundation for Innovation (CFI), the Brazilian Ministry of Science, Technology, and Innovations, the International Center for Theoretical Physics South American Institute for Fundamental Research (ICTP-SAIFR), the Research Grants Council of Hong Kong, the National Natural Science Foundation of China (NSFC), the Israel Science Foundation (ISF), the US-Israel Binational Science Fund (BSF), the Leverhulme Trust, the Research Corporation, the National Science and Technology Council (NSTC), Taiwan, the United States Department of Energy, and the Kavli Foundation. The authors gratefully acknowledge the support of the NSF, STFC, INFN and CNRS for provision of computational resources.

This work was supported by MEXT, the JSPS Leading-edge Research Infrastructure Program, JSPS Grant-in-Aid for Specially Promoted Research 26000005, JSPS Grant-in-Aid for Scientific Research on Innovative Areas 2402: 24103006, 24103005, and 2905: JP17H06358, JP17H06361 and JP17H06364, JSPS Core-to-Core Program A. Advanced

Research Networks, JSPS Grants-in-Aid for Scientific Research (S) 17H06133 and 20H05639, JSPS Grant-in-Aid for Transformative Research Areas (A) 20A203: JP20H05854, the joint research program of the Institute for Cosmic Ray Research, University of Tokyo, the National Research Foundation (NRF), the Computing Infrastructure Project of the Global Science experimental Data hub Center (GSDC) at KISTI, the Korea Astronomy and Space Science Institute (KASI), the Ministry of Science and ICT (MSIT) in Korea, Academia Sinica (AS), the AS Grid Center (ASGC) and the National Science and Technology Council (NSTC) in Taiwan under grants including the Science Vanguard Research Program, the Advanced Technology Center (ATC) of NAOJ, and the Mechanical Engineering Center of KEK.

For the purpose of open access, the authors have applied a Creative Commons Attribution (CC BY) license to any Author Accepted Manuscript version arising. We request that citations to this article use 'A. G. Abac *et al.* (LIGO-Virgo-KAGRA Collaboration), ...' or similar phrasing, depending on journal convention.

SUPPLEMENTAL MATERIAL

Significance estimation for a non-negative QNM amplitude

In the main text we quote the significance with which the amplitude A of a given QNM is shown to be > 0 . We use the one-dimensional highest posterior density (HPD) credible regions based on samples drawn from the posterior density. The one dimensional p HPD is the shortest interval that contains a fraction p of the samples. It can be computed by considering the $\lfloor (1-p)N \rfloor$ intervals in the sorted samples that each include $\lceil pN \rceil$ samples, where N is the total number of samples available, and choosing the shortest one (i.e. the one with the highest estimated density). Using sample-based HPD intervals in this way can produce significant differences between the true and estimated interval when $p \simeq 1/N$ [2], but in all cases in this paper, we have sufficient samples so that $pN \gg 1$, and this is not an issue.

To convert a p HPD into a significance level, $x\sigma$, we relate these quantities through the Gaussian distribution, via

$$p = \int_{-x}^x dy \phi(y), \quad (3)$$

where $\phi(y)$ is the standard normal density. For example, a 3σ interval contains a fraction $p = 0.9973$ of the samples.

Validity regimes of QNM models

Analyses of NR simulations of BBH mergers, like GW250114, with Eq. (1) show that the time interval in which fits at consecutive start times yield exponentially consistent amplitudes varies based on the mode content [106, 221, 222]. To determine when Eq. (1) is valid for the models we consider, we study the equal-mass, non-spinning NR BBH simulation SXS:BBH:3617 [223, 224], whose intrinsic parameters lie within the 90% credible region of GW250114. For each QNM model, we perform a linear least-squares fit to the (2, 2) mode with the start times $t_> \in [0, 40]t_{M_f}$ in steps of $0.1t_{M_f}$ and measure the complex amplitude of each QNM at t_{peak} [225]. We define a stability window of size $10t_{M_f}$ as a region in which the QNMs in the model have amplitudes whose fractional variation is comparable to our 50% credible level measurement uncertainties in GW250114 (14% for the 220 at $t_> = 11t_{M_f}$ with the 220 model, 24% for the 221 at $t_> = 6t_{M_f}$ with the 220+221 model, and 40% for the 222 at $t_> = 3t_{M_f}$ with the 220+221+222 model; these times are chosen based on the value used in Abac *et al.* [2] and the times identified in Fig. 7) and whose values agree with the most stable value to the same uncertainty. We define the stability regime as the union of all such windows. For the 220, 220+221, 220+221+222 models, we find these regimes to be approximately $[11, 40]t_{M_f}$, $[6, 34]t_{M_f}$, and $[3, 22]t_{M_f}$.

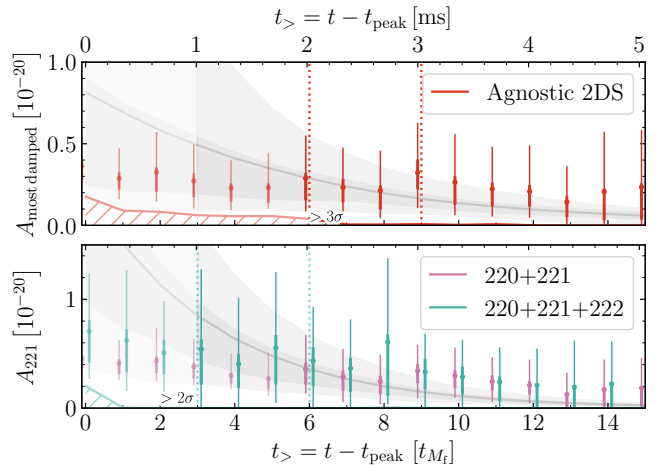


FIG. 7. Consistency of a NR-simulation's post-merger data with two QNMs. Identical to Fig. 1, but instead for a simulated signal using the equal-mass, non-spinning NR BBH simulation SXS:BBH:3617 with Gaussian noise; fits are performed with ringdown.

Comparison to NR-informed predictions

In Fig. 1, we have found that at least two agnostic damped sinusoids are required to explain the post-merger signal, and when assuming a Kerr remnant, we have observed that the 221 amplitudes remain non-zero at $> 3\sigma$ up to $9t_{M_f}$ after the peak. Here, we find similar results when employing a simulated signal of the NR simulation SXS:BBH:3617 [223, 224]. The signal is injected into Gaussian noise generated using the power spectral density estimated from GW250114, with extrinsic parameters set to the preliminary-reference maximum-likelihood values inferred using NRSur7dq4 [2]. We generate 10 different noise realizations and choose the one such that the analysis of the simulated signal most closely resembles that obtained for GW250114. Like in Fig. 1, we find (see upper panel in Fig. 7) that at around $t_> \gtrsim 9t_{M_f}$ the amplitude of the more rapidly decaying damped sinusoid becomes consistent with zero at the 90% level. Furthermore, at around $t_> \lesssim 6t_{M_f}$ (lower panel), the amplitude of the 221 mode in the 220+221 model also starts to deviate from its extrapolated values; but, by adding the 222 mode to the fit one can again recover amplitude consistency at early times around $t_> \gtrsim 3t_{M_f}$.

We perform another test to verify that the relative amplitudes and phases of the 220 and 221 QNMs are consistent with predictions from NR. This requires mapping the detector QNM amplitudes in Eq. (1) to the remnant-frame QNM amplitudes, with which the strain over the two-sphere in the remnant frame can be written as

$$h \equiv h_+ - ih_\times = \sum_{\substack{\ell \geq 2 \\ -\ell \leq m \leq \ell \\ n \geq 0}} C_{\ell m n} e^{-i\omega_{\ell m n} t} {}_{-2}S_{\ell m n}(M_f \chi_f \omega_{\ell m n}, \theta_{JN}, \varphi), \quad (4)$$

where $\omega_{\ell m n} \equiv 2\pi f_{\ell m n} - i/\tau_{\ell m n}$ and ${}_{-2}S_{\ell m n}(M_f \chi_f \omega_{\ell m n}, \theta_{JN}, \varphi)$ is

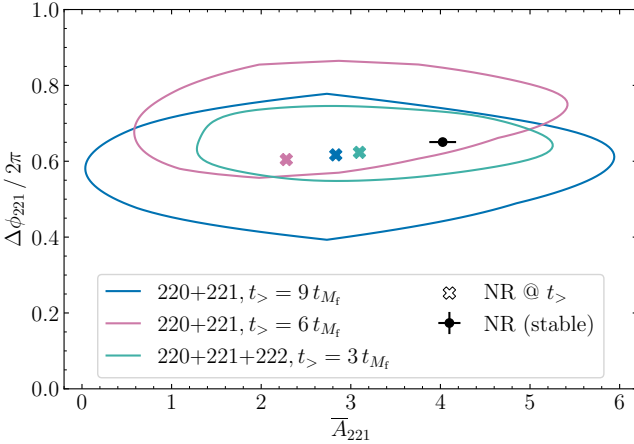


FIG. 8. Consistency of the 220 and 221 QNMs from GW250114 with NR predictions. The 50% credible regions of the two-dimensional posteriors on $\Delta\phi_{221}$ and \bar{A}_{221} for GW250114, at varying fit start times, as measured by ringdown. Colored crosses represent fits to the equal-mass, non-spinning NR BBH simulation SXS:BBH:3617. For $t_> = t - t_{\text{peak}}[t_{M_f}] \in \{6, 9\}t_{M_f}$ the 220+221 model is used, while for $t_> = 3t_{M_f}$, the 220+221+222 model is used. The black marker represents a stable value of these quantities over a window ranging from $t_> \in [12, 22]t_{M_f}$, with the data point the mean and the error bars the 1σ variation over said window.

the spin-weight -2 $\ell m n$ spheroidal harmonic with oblateness $M_f \chi_f \omega_{\ell m n}$ and evaluation point on the two-sphere (θ_{JN}, φ) . The complex amplitudes $C_{\ell m n}$ in Eq. (4) are related to the complex amplitudes in Eq. (1) via [109]

$$C_{\ell+|m|n-2} S_{\ell+|m|n}(\theta_{JN}, \varphi) = A_{\ell m n}^R, \quad (5a)$$

$$C_{\ell-|m|n-2} S_{\ell-|m|n}(\theta_{JN}, \varphi) = A_{\ell m n}^L. \quad (5b)$$

However, because A_{220}^R is measured to be larger than A_{220}^L for this event, from here on we focus exclusively on the $\ell|m|n$ QNMs. Using the QNM amplitudes over the two-sphere, we can compare the relative amplitudes and phases of the 220 and 221 QNMs via

$$\bar{A}_{221} = \left| \frac{C_{221}}{C_{220}} \right|, \quad (6a)$$

$$\Delta\phi_{221} = \arg \left[\frac{C_{221}}{C_{220}} \right]. \quad (6b)$$

The quantities $\bar{A}_{\ell m n}$ and $\Delta\phi_{\ell m n}$ should be interpreted as the amplitude ratio and phase difference between the 220 and 221 QNMs on the two-sphere extrapolated to t_{peak} . Each contour in Fig. 8 shows the 50% credible region for the fit performed at the start time indicated in the legend. For $t_> \in \{6, 9\}t_{M_f}$ the 220+221 model is used, while for $t_> = 3t_{M_f}$, the 220+221+222 model is used. The corresponding crosses represent the values extracted from fits to the NR simulation SXS:BBH:3617 performed using a linear least-squares fit to the $(2, 2)$ mode [225]. The marker with error bars is obtained by fitting the 220+221+222 model over a $10t_{M_f}$ window in which these quantities have stabilized. That is, we fit the NR

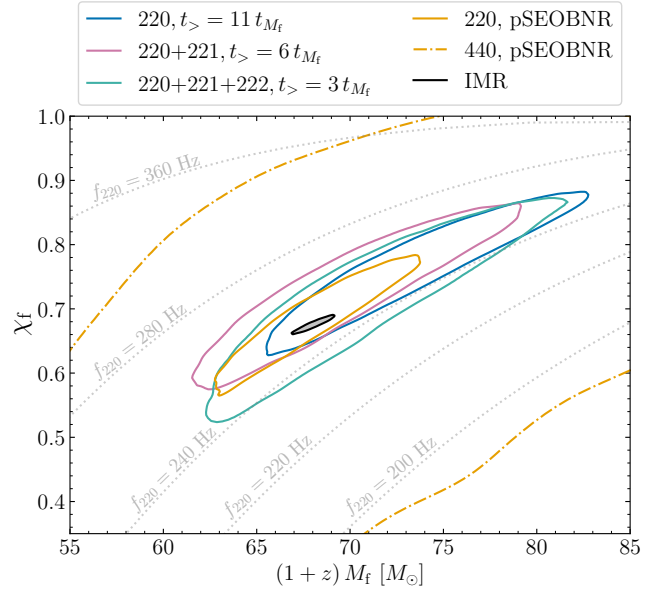


FIG. 9. Final mass and spin consistency. The 90% credible regions of the remnant mass and spin inferred from a series of ringdown fits with pyRing: using the 220 model at $t_> = 11t_{M_f}$, the 220+221 model at $t_> = 6t_{M_f}$, and the 220+221+222 model at $t_> = 3t_{M_f}$. We also show results for the 220 and 440 modes with the pSEOBNR analysis, as well as the IMR results of the full signal.

waveform at times $t_> \in [12, 22]t_{M_f}$ —the latest $10t_{M_f}$ contained in the regime of validity for the 220+221+222 model, measure the mean and standard deviation of C_{220} and C_{221} over said $10t_{M_f}$ window, and then compute \bar{A}_{221} and $\Delta\phi_{221}$ accordingly. As can be seen, from $t_> \in [3, 9]t_{M_f}$ the amplitudes and phases extracted from the data are broadly consistent with the values predicted. More specifically, they are consistent with the most stable value to $\geq 38\%$ credibility. Their values evolve because the amplitudes of the exponentially damped-sinusoid model that are used are insufficient to recover particularly stable overtone amplitudes for these $t_>$ values at effectively infinite SNR.

Overall, these results indicate that the 221 amplitudes and phases measured from GW250114 when using different ringdown models at different starting times are consistent with expectations from a BBH in GR.

Final mass and spin consistency

In Fig. 9 we show the mass and spin posteriors obtained from the 220, 220+221, and 220+221+222 model fits at $t_> = 11t_{M_f}$, $t_> = 6t_{M_f}$, and $t_> = 3t_{M_f}$, and from the 220 and 440 pSEOBNR model. For all these fits, the inferred mass and spin are consistent with that from the full IMR analysis at 90% credibility.

Detectability of quadrupolar first overtone via model selection

In the main text, we have assessed QNM detectability based on the posterior amplitude support away from zero. A complementary criterion is represented by the Bayes factor, which quantifies the ratio of the evidences of competing models, with each evidence defined as the integral of the likelihood weighted by the prior [226]. In Fig. 10, we show the \log_{10} Bayes factors of the two-mode model compared to the one-mode model over time. The results from `pyRing` are obtained from the `cpnest` nested sampler used in inference [192], while the ones from `ringdown` are estimated from the 221 amplitudes using the Savage–Dickey ratio [227]. For nested models, these two approaches are equivalent [228]. For Savage–Dickey, we derive the amplitude maximum prior from the `pyRing` maximum priors on the right- and left-handed polarized contributions of the modes (between $[0, 5 \times 10^{-20}]$) combined with the spin-weighted spherical harmonics [2]. The reported values correspond to the median and 90% credible interval of 1000 Bayes factor estimates with bootstrap resamples of the amplitude samples. The `pyRing` uncertainties are not displayed since they are comparable to the marker size; they represent the half-width of the 90% credible interval estimated from the four nested sampling chains.

We find positive evidence for the presence of the 221 as late as $8t_{M_f}$ ($9t_{M_f}$) from `pyRing` (`ringdown`), with \log_{10} Bayes factors of $0.56^{+0.26}_{-0.26}$ ($2.51^{+0.36}_{-0.29}$) at $6t_{M_f}$, $2.38^{+0.31}_{-0.31}$ ($3.47^{+2.02}_{-0.50}$) at $8t_{M_f}$ and $-0.53^{+0.31}_{-0.31}$ ($0.20^{+0.09}_{-0.08}$) at $9t_{M_f}$. A similar trend is observed using agnostic sinusoids. The presence of a second overtone 222 is not significantly preferred at any time. These results are in agreement with the QNMRF detection statistics in Fig. 3, as well as with the non-zero amplitude consistency in Fig. 1, as discussed in the main text. They are also in accord with predictions from analysis of similarly loud simulated signals [229].

The difference between the two pipelines is due to different prior volumes and data length used. In fact, we are able to obtain the same values within the Bayes factor uncertainty when analyzing with `pyRing` 0.6 s of data with similar priors to `ringdown`, and when running `ringdown` on the same `pyRing` settings. For a complete description of the differences in settings between the codes, see Supplemental Material in Abac *et al.* [2].

QNM rational filter

The QNMRF analysis [116] is designed to isolate and remove specific complex-valued QNMs from the ringdown signal in the frequency domain. The resulting residual is then compared to pure colored Gaussian noise [117, 118]. The filter is constructed for a given set of QNMs, corresponding to specific BH masses and spins.

QNMRF computes the mode detection statistic, \mathcal{D} , defined as a comparison between two ringdown model hypotheses: \mathcal{H} , which includes an additional mode, and \mathcal{H}' , which excludes

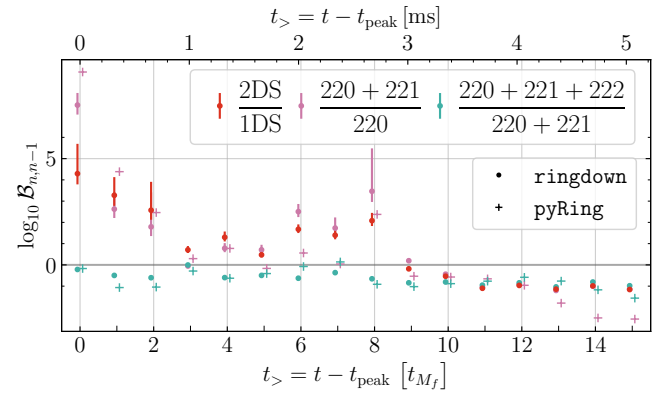


FIG. 10. Consistency of post-merger data with two QNMs via model selection. The Bayes factors comparing the analyzed QNM model to a nested model with one fewer mode. Dots indicate the estimated `ringdown` Bayes factor and plus the `pyRing` Bayes factor.

it. \mathcal{D} is analogous to a logarithmic Bayes factor, yet differs from the Bayes factors used in other time-domain ringdown analyses [119]. To assess statistical significance, we then take a frequentist approach to estimate FAPs due to the background noise, and determine a threshold, $\mathcal{D}_{1\%}$, corresponding to a 1% FAP. Given the data d , the statistic is expressed as:

$$\mathcal{D}(\mathcal{H} : \mathcal{H}') = \log_{10} \frac{\mathcal{Z}(d|\mathcal{H})}{\mathcal{Z}(d|\mathcal{H}')}, \quad (7)$$

where $\mathcal{Z}(d|\mathcal{H})$ and $\mathcal{Z}(d|\mathcal{H}')$ denote the evidences under hypotheses \mathcal{H} and \mathcal{H}' .

In Fig. 3, the pink crosses represent the offset of $\mathcal{D}[\mathcal{H}(220 + 221) : \mathcal{H}'(220)]$ relative to the 1% FAP threshold evaluated on background noise, while the green plus indicate the offset of $\mathcal{D}[\mathcal{H}(220 + 221 + 222) : \mathcal{H}'(220 + 221)]$ relative to its corresponding threshold.

For each ringdown model hypothesis, we also compute the joint posterior quantile $p(M_f^{\text{IMR}}, \chi_f^{\text{IMR}})$ of the remnant BH mass and spin, inferred from the full IMR analysis, using `NRSur7dq4`. This credible contour represents the region on which the inferred parameters $(M_f^{\text{IMR}}, \chi_f^{\text{IMR}})$ lie, serving as a consistency check with the IMR results [119]. A lower p value indicates a better match between the IMR analysis and the given QNM hypothesis. Among all possible additional modes added to the nested model, one at a time, the mode that (i) yields a detection statistic \mathcal{D} above the threshold and simultaneously (ii) results in the greatest reduction in $p(M_f^{\text{IMR}}, \chi_f^{\text{IMR}})$ is considered confidently identified for a given starting time. In Fig. 3, when the two-mode model $\mathcal{H}(220 + 221)$ is favored over the single-mode model $\mathcal{H}'(220)$, i.e. when $\mathcal{D}[\mathcal{H}(220 + 221) : \mathcal{H}'(220)] > \mathcal{D}_{1\%}$, we find that the corresponding joint posterior quantile $p(M_f^{\text{IMR}}, \chi_f^{\text{IMR}})$ also decreases across starting times from $4t_{M_f}$ to $10t_{M_f}$, indicating improved consistency with the IMR-inferred remnant parameters. Similarly, when the three-mode model $\mathcal{H}(220 + 221 + 222)$ is preferred over $\mathcal{H}'(220 + 221)$ with $\mathcal{D} > \mathcal{D}_{1\%}$ from starting times $1t_{M_f}$ to $5t_{M_f}$, we observe a reduction in $p(M_f^{\text{IMR}}, \chi_f^{\text{IMR}})$. These results

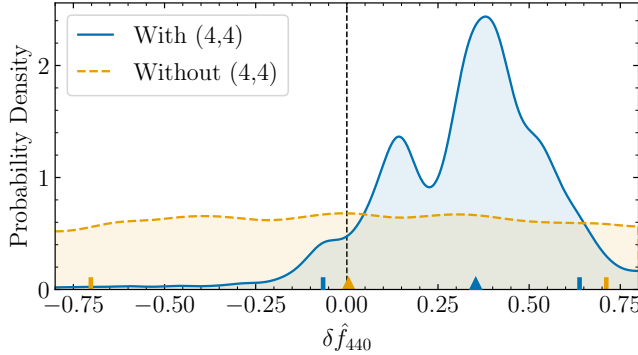


FIG. 11. Validation of the 440-mode constraint using simulated signals. Posterior distributions for the fractional deviation in the 440 QNM frequency, $\delta\hat{f}_{440}$, obtained from simulated NR signals consistent with GW250114. The blue curve shows results for a simulated signal that includes the $(\ell, |m|) = (4, 4)$ multipoles, while the orange curve corresponds to a simulated signal with the modes removed. Triangles mark the median values and vertical bars the symmetric 90% credible interval.

suggest that these additional modes enhance the fit to the data and also improve the IMR consistency.

Validation of the $(4, 4)$ fundamental-mode frequency constraint

To validate the constraint on the 440 QNM frequency, we perform targeted simulated-signal studies, recovering the signals using the pSEOBNR model. We analyze a synthetic signal generated using the equal-mass, non-spinning NR simulation SXS:BBH:3617 [217, 223, 224], with extrinsic parameters compatible with GW250114, and injected into Gaussian noise. Several features observed in the real GW250114 data, particularly those associated with the 440 QNM, can be qualitatively reproduced in this Gaussian noise injection. As shown in Fig. 11, the 440 QNM frequency is recovered with comparable precision to the real-signal analysis, while the damping time remains largely unconstrained.

In both the real event and Gaussian-noise injections, the posterior for $\delta\hat{f}_{440}$ can exhibit a multimodal structure, especially under a wide, uninformative prior for $\delta\hat{f}_{440}$. By contrast, an analogous injection into zero-noise data yields posteriors peaked at $\delta\hat{f}_{440} = 0$ with no significant substructure. The observed multimodality in $\delta\hat{f}_{440}$ is primarily driven by samples with large values of $\delta\hat{f}_{440}$, corresponding to long-lived, nearly sinusoidal modes. Indeed, for a purely sinusoidal signal, the likelihood is expected to exhibit secondary maxima with regular spacing in frequency [230]. When using an extended prior allowing for $\delta\hat{f}_{440}$ values up to 4, multimodality in $\delta\hat{f}_{440}$ is clearly associated with large $\delta\hat{f}_{440}$ samples. The maximum-likelihood parameters lie near the GR-consistent central mode, indicating that the secondary peaks are not favored by the data. Given the low SNR in the 440 mode, we do not expect to constrain deviations to its damping time. For

the main results shown in Fig. 4, we adopt a uniform prior on $\delta\hat{f}_{440} \in [-0.8, 0.8]$ consistent with that used for the ringdown constraints on the 221 mode.

Finally, we repeat the Gaussian-noise injection, using the same NR simulation and parameters, but with the $(\ell, |m|) = (4, 4)$ multipoles explicitly removed from the signal. In this case, the resulting constraint on $\delta\hat{f}_{440}$ is uninformative (orange curve in Fig. 11) suggesting that the posteriors recovered in the full injections are driven by the presence of the $(4, 4)$ multipoles in the data. These findings reinforce the interpretation that the constraint on $\delta\hat{f}_{440}$ obtained from GW250114 reflects a genuine physical feature of the signal rather than an artifact of the analysis or noise.

Principal component analysis

A limitation of the FTI and TIGER results presented above is that individual PN deformation parameters are varied one at a time with all other parameters being fixed to the GR baseline. Whilst robust [158], single-parameter tests do not probe correlations across multiple PN orders, potentially missing more complex departures from GR. An alternative scheme was proposed in [164, 165], in which six PN deformation parameters are simultaneously varied, taken to be the 1.5PN to the 3.5PN parameters. The -1PN , 0PN , 0.5PN , and 1PN terms are fixed to their GR values. The approach is to estimate the joint posterior for the standard binary parameters plus the 6 PN deformation parameters. Then, one marginalizes over the GR parameters to yield a six-dimensional posterior for the PN deformations that captures correlated deviations [162–165], though strong parameter correlations can often render the posteriors uninformative or weakly constrained. Priors on the deformation parameters are taken to be uniform, such that $\delta\hat{\varphi}_{\text{prior}}^{(i)} \sim \mathcal{U}(-20, 20)$.

To mitigate against this potential shortcoming, we apply a PCA to the six-dimensional posteriors, diagonalize the covariance matrix and identify the linear combination of PN deformation parameters that are best constrained by the data [164, 165]. The new basis, $\delta\hat{\varphi}_{\text{PCA}}^{(i)}$, provides orthogonal directions that minimize posterior widths. The PCA analysis is applied to the TIGER framework, using `IMRPhenomXPHM_SpinTaylor` [160, 161], and the FTI framework, using `SEOBNRv5HM_ROM` [125]. We find that the leading two PCA parameters are informative using the TIGER pipeline, and the leading three when using FTI, with all tests being consistent with zero. The 90% credible bounds on the leading PCA parameter $\delta\hat{\varphi}_{\text{PCA}}^{(1)}$ for GW250114 are $-0.01^{+0.02}_{-0.02}$ (FTI) and $0.02^{+0.05}_{-0.05}$ (TIGER) respectively. The leading and sub-leading PCA parameters can be re-expressed as weighted combinations of the PN deformation coefficients. From the

FTI analysis of GW250114, we find

$$\begin{aligned}\delta\hat{\varphi}_{\text{PCA}}^{(1)} &= 0.7482 \delta\hat{\varphi}_3 - 0.1337 \delta\hat{\varphi}_4 + 0.4910 \delta\hat{\varphi}_{5l} \\ &\quad - 0.3797 \delta\hat{\varphi}_6 + 0.0240 \delta\hat{\varphi}_{6l} + 0.1908 \delta\hat{\varphi}_7, \quad (8a)\end{aligned}$$

$$\begin{aligned}\delta\hat{\varphi}_{\text{PCA}}^{(2)} &= 0.6387 \delta\hat{\varphi}_3 + 0.0139 \delta\hat{\varphi}_4 - 0.4136 \delta\hat{\varphi}_{5l} \\ &\quad + 0.5397 \delta\hat{\varphi}_6 + 0.0235 \delta\hat{\varphi}_{6l} - 0.3592 \delta\hat{\varphi}_7. \quad (8b)\end{aligned}$$

The PCA coefficients are dominated by the 1.5PN, 2.5PN log, and 3PN terms, in broad agreement with the individual PN coefficient analysis, as seen in Fig 5. This analysis demonstrates that even when allowing for correlated deviations across multiple PN orders, the deviations away from GR inferred from GW250114 alone are constrained to be negligible.

Bounds on the black hole area theorem

A key outcome of Abac *et al.* [2] was a precision constraint on Hawking's area theorem [172], a fundamental consequence of the second law of BH mechanics stating that the horizon area of a BH cannot decrease over time. In practice, this implies that for BH mergers, the area of the final remnant must exceed the combined area of the two progenitor BHs [172]. Analogously to Abac *et al.* [2], we test this prediction by independently estimating the initial and final BH areas using different portions of the signal; however, differently from Abac *et al.* [2], we employ the entire signal, whereas in the other analysis the data around merger are excluded. Our approach closely follows the IMR consistency test. We constrain the masses and spins of the BHs in the inspiral and post-inspiral phases, which we directly map to the initial and final areas.

The areas are calculated using the Kerr formula [19]

$$\mathcal{A}(m, \chi) = 8\pi \left(\frac{Gm}{c^2} \right)^2 \left(1 + \sqrt{1 - \chi^2} \right), \quad (9)$$

where m and χ are the BH mass and dimensionless spin. For the initial area \mathcal{A}_i , we infer the individual BH masses and spins from the inspiral, and the total area is calculated as $\mathcal{A}_i = \mathcal{A}_1 + \mathcal{A}_2$. For the final area \mathcal{A}_f , we employ NR calibrated fits to estimate the remnant BH mass and spin from the progenitor parameters [126, 127], emphasizing that the initial BH source properties used in this calculation are inferred exclusively from post-inspiral data. In Fig. 12, we show the fractional difference between the final and initial areas, $(\mathcal{A}_f - \mathcal{A}_i)/\mathcal{A}_i$. We find that GW250114 is consistent with the area theorem at the $4.8\sigma_{\text{IMRCT}}$ credibility level. Here, the significance $X\sigma_{\text{IMRCT}}$ is calculated from the difference in areas and defined as the ratio of the difference in means to the standard deviation of the differences [2],

$$X = \frac{\mu_f - \mu_i}{\sqrt{\sigma_f^2 + \sigma_i^2}}, \quad (10)$$

which expresses how many standard deviations the observed mean deviates from zero. Here μ_i and μ_f denote the means

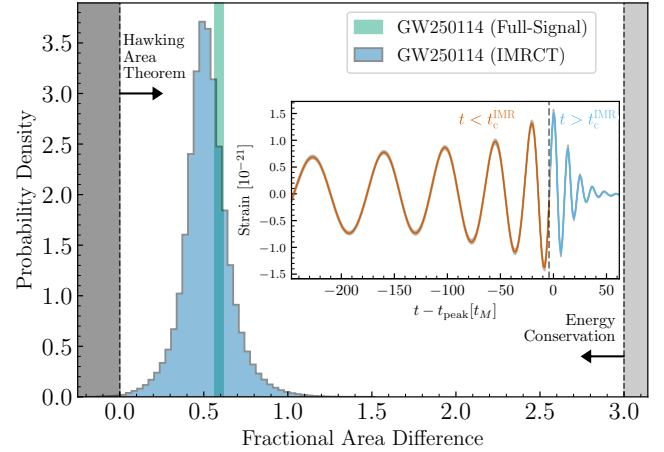


FIG. 12. BH area-law test using the entirety of GW250114. The fractional difference between the area of the final BH \mathcal{A}_f and the total area of the initial BH's \mathcal{A}_i as calculated using the IMR consistency test on GW250114. The grey shaded region on the left marks the region in which the area theorem is violated, $(\mathcal{A}_f - \mathcal{A}_i)/\mathcal{A}_i < 0$. The grey shaded region on the right highlights the region excluded by energy conservation $M_f \leq m_1 + m_2$. The vertical green band is the 90% credible interval inferred from the full-signal analysis in Abac *et al.* [2]. The inset schematically shows a reconstructed (grey) signal in LIGO Livingston using the full-signal analysis [2], along with the inspiral (orange) and post-inspiral (light blue) regions used in the IMR consistency test, such that the time t_c^{IMR} corresponds to the transition frequency f_c^{IMR} , noting that the data is split in the frequency-domain and not the time-domain.

of the initial and final areas respectively, while σ_i and σ_f are their corresponding standard deviations. As discussed in Abac *et al.* [2], this estimate is less sensitive to sampling errors in the distribution tails since it relies only on the first two cumulants. This bound is slightly more stringent than that presented in Abac *et al.* [2], due to stronger GR assumptions and use of the complete signal. Moreover, the test performed here splits the data in the frequency-domain, which is not equivalent to the time-domain analysis done in Abac *et al.* [2]. Using the fractional difference to calculate the significance, we find $3.7\sigma_{\text{IMRCT}}$, with differences being driven by uncertainty in the initial area normalization. In Fig. 12, we also show the 90% credible interval from the full-signal analysis using NRSur7dq4 [2], which coherently describe the complete signal assuming both GR and the area theorem. It yields the most stringent bound because it employs the full SNR of GW250114, instead of using a smaller portion associated either to the inspiral or the post-inspiral phases.

Residuals test

The residuals test [35] is a statistical analysis that checks for the presence of excess coherent power remaining in the detector network after subtracting the best-fit waveform from the data [173, 174]. Significant residual power could indicate the

presence of additional physical effects that are not captured by current BBH models, modeling systematics, or unaccounted instrumental noise artifacts.

We perform the residual data by subtracting from the original data the maximum-likelihood NRSur7dq4 waveform model. If the model adequately captures the GW signal, the resulting residuals should be consistent with stationary Gaussian noise. The residual data is then analyzed using BayesWave [188], and the 90% credible upper limit on the network SNR ρ_{90} is calculated. To compare this ρ_{90} with its expected distribution, segments of data around the signal (with no injected signal) are also analyzed and the probability of obtaining an ρ_{90} higher than that of the residual data is calculated and reported as the p -value = $P(\rho''_{90} \geq \rho_{90})$, where ρ''_{90} is the 90% credible upper limit on the coherent SNR of the background, noise-only segments.

A higher p -value suggests that the residual power is more consistent with instrumental noise, indicating insufficient evidence to reject the null hypothesis that the residual power originates from noise. For a single event, we also expect the p -value to be a random draw from a uniform distribution on the interval (0,1]. Furthermore, the goodness of fit of the GR template for the signal in the data can be quantified by calculating the 90% credible lower limit on the fitting factor (FF), given by:

$$\text{FF}_{90} = \frac{\rho_{\text{GR}}}{\sqrt{\rho_{\text{GR}}^2 + \rho_{90}^2}}, \quad (11)$$

where ρ_{GR} is the optimal network SNR for the maximum-likelihood waveform [134].

For GW250114, we find that $\rho_{90} = 6.86$ with a p -value of 0.34. The calculated FF₉₀ is 0.996. Based on this, we do not find any significant coherent power beyond what is expected from noise.

general relativity, *Gen. Rel. Grav.* **40**, 1997 (2008), arXiv:gr-qc/0405109.

- [8] Y. Foures-Bruhat, Theoreme d'existence pour certains systemes derivees partielles non lineaires, *Acta Mat.* **88**, 141 (1952).
- [9] K. Schwarzschild, On the gravitational field of a mass point according to Einstein's theory, *Sitzungsber. Preuss. Akad. Wiss. Berlin (Math. Phys.)* **1916**, 189 (1916), arXiv:physics/9905030.
- [10] E. T. Newman, E. Couch, K. Chinnapared, A. Exton, A. Prakash, and R. Torrence, Metric of a Rotating, Charged Mass, *J. Math. Phys.* **6**, 918 (1965).
- [11] W. Israel, Event horizons in static electrovac space-times, *Commun. Math. Phys.* **8**, 245 (1968).
- [12] B. Carter, Axisymmetric Black Hole Has Only Two Degrees of Freedom, *Phys. Rev. Lett.* **26**, 331 (1971).
- [13] S. W. Hawking, Black holes in general relativity, *Commun. Math. Phys.* **25**, 152 (1972).
- [14] D. C. Robinson, Uniqueness of the Kerr black hole, *Phys. Rev. Lett.* **34**, 905 (1975).
- [15] P. O. Mazur, Proof of uniqueness of the Kerr-Newman black hole solution, *J. Phys. A* **15**, 3173 (1982).
- [16] B. Carter, Global structure of the Kerr family of gravitational fields, *Phys. Rev.* **174**, 1559 (1968).
- [17] R. Penrose, Gravitational collapse: The role of general relativity, *Riv. Nuovo Cim.* **1**, 252 (1969).
- [18] R. Penrose and R. M. Floyd, Extraction of rotational energy from a black hole, *Nature* **229**, 177 (1971).
- [19] J. M. Bardeen, B. Carter, and S. W. Hawking, The Four laws of black hole mechanics, *Commun. Math. Phys.* **31**, 161 (1973).
- [20] M. Schmidt, 3C 273 : A Star-Like Object with Large Red-Shift, *Nature* **197**, 1040 (1963).
- [21] M. Dafermos, G. Holzegel, and I. Rodnianski, The linear stability of the Schwarzschild solution to gravitational perturbations, *Acta Mat.* **222**, 1 (2019), arXiv:1601.06467 [gr-qc].
- [22] R. Teixeira da Costa, Mode stability for the Teukolsky equation on extremal and subextremal Kerr spacetimes, *Commun. Math. Phys.* **378**, 705 (2020), arXiv:1910.02854 [gr-qc].
- [23] S. Klainerman and J. Szeftel, Kerr stability for small angular momentum, *Pure Appl. Math. Quart.* **19**, 791 (2023), arXiv:2104.11857 [math.AP].
- [24] M. Dafermos, G. Holzegel, I. Rodnianski, and M. Taylor, The non-linear stability of the Schwarzschild family of black holes, arXiv:2104.08222 [gr-qc] (2021).
- [25] S. W. Hawking and R. Penrose, The Singularities of gravitational collapse and cosmology, *Proc. Roy. Soc. Lond. A* **314**, 529 (1970).
- [26] A. Almheiri, T. Hartman, J. Maldacena, E. Shaghoulian, and A. Tajdini, The entropy of Hawking radiation, *Rev. Mod. Phys.* **93**, 035002 (2021), arXiv:2006.06872 [hep-th].
- [27] S. Raju, Lessons from the information paradox, *Phys. Rept.* **943**, 1 (2022), arXiv:2012.05770 [hep-th].
- [28] C. M. Will, The Confrontation between General Relativity and Experiment, *Living Rev. Relativity* **17**, 4 (2014), arXiv:1403.7377 [gr-qc].
- [29] E. Berti *et al.*, Testing General Relativity with Present and Future Astrophysical Observations, *Class. Quantum Grav.* **32**, 243001 (2015), arXiv:1501.07274 [gr-qc].
- [30] N. Yunes, X. Siemens, and K. Yagi, Gravitational-Wave Tests of General Relativity with Ground-Based Detectors and Pulsar-Timing Arrays, *Living Rev. Relativity* **28**, 3 (2025), arXiv:2408.05240 [gr-qc].
- [31] A. G. Abac *et al.* (LIGO Scientific, VIRGO, KAGRA), GWTC-4.0: An Introduction to Version 4.0

* lvc.publications@ligo.org

- [1] J. Aasi *et al.* (LIGO Scientific Collaboration), Advanced LIGO, *Class. Quantum Grav.* **32**, 074001 (2015), arXiv:1411.4547 [gr-qc].
- [2] A. G. Abac *et al.*, GW250114: testing Hawking's area law and the Kerr nature of black holes, arXiv:2509.00000 [gr-qc] (2025).
- [3] F. Acernese *et al.* (Virgo Collaboration), Advanced Virgo: a second-generation interferometric gravitational wave detector, *Class. Quantum Grav.* **32**, 024001 (2015), arXiv:1408.3978 [gr-qc].
- [4] T. Akutsu *et al.* (KAGRA), Overview of KAGRA: Detector design and construction history, *PTEP* **2021**, 05A101 (2021), arXiv:2005.05574 [physics.ins-det].
- [5] A. Einstein, On the General Thoery of Relativity, *Sitzungsber. K. Preuss. Akad. Wiss.* **49**, 778 (1915).
- [6] R. P. Kerr, Gravitational field of a spinning mass as an example of algebraically special metrics, *Phys. Rev. Lett.* **11**, 237 (1963).
- [7] R. L. Arnowitt, S. Deser, and C. W. Misner, The Dynamics of

of the Gravitational-Wave Transient Catalog, (2025), arXiv:2508.18080 [gr-qc].

[32] GWTC-4.0: Updating the Gravitational-Wave Transient Catalog with Observations from the First Part of the Fourth LIGO-Virgo-KAGRA Observing Run, (2025), arXiv:2508.18082 [gr-qc].

[33] L. Blanchet and B. S. Sathyaprakash, Detecting a Tail Effect in Gravitational-Wave Experiments, *Physical Review Letters* **74**, 1067 (1995).

[34] B. P. Abbott *et al.* (LIGO Scientific Collaboration, Virgo Collaboration), Observation of Gravitational Waves from a Binary Black Hole Merger, *Phys. Rev. Lett.* **116**, 061102 (2016), arXiv:1602.03837 [gr-qc].

[35] B. P. Abbott *et al.* (LIGO Scientific, Virgo), Tests of general relativity with GW150914, *Phys. Rev. Lett.* **116**, 221101 (2016), [Erratum: *Phys. Rev. Lett.* **121**, 129902 (2018)], arXiv:1602.03841 [gr-qc].

[36] B. P. Abbott *et al.* (LIGO Scientific Collaboration, Virgo Collaboration), GWTC-1: A Gravitational-Wave Transient Catalog of Compact Binary Mergers Observed by LIGO and Virgo during the First and Second Observing Runs, *Phys. Rev. X* **9**, 031040 (2019), arXiv:1811.12907 [astro-ph.HE].

[37] R. Abbott *et al.* (LIGO Scientific, Virgo), GWTC-2: Compact Binary Coalescences Observed by LIGO and Virgo During the First Half of the Third Observing Run, *Phys. Rev. X* **11**, 021053 (2021), arXiv:2010.14527 [gr-qc].

[38] R. Abbott *et al.* (LIGO Scientific, Virgo), GWTC-2.1: Deep extended catalog of compact binary coalescences observed by LIGO and Virgo during the first half of the third observing run, *Phys. Rev. D* **109**, 022001 (2024), arXiv:2108.01045 [gr-qc].

[39] R. Abbott *et al.* (KAGRA, Virgo, LIGO Scientific), GWTC-3: Compact Binary Coalescences Observed by LIGO and Virgo during the Second Part of the Third Observing Run, *Phys. Rev. X* **13**, 041039 (2023), arXiv:2111.03606 [gr-qc].

[40] B. P. Abbott *et al.* (LIGO Scientific, Virgo), Tests of General Relativity with GW170817, *Phys. Rev. Lett.* **123**, 011102 (2019), arXiv:1811.00364 [gr-qc].

[41] B. P. Abbott *et al.* (LIGO Scientific Collaboration, Virgo Collaboration), Tests of General Relativity with the Binary Black Hole Signals from the LIGO-Virgo Catalog GWTC-1, *Phys. Rev. D* **100**, 104036 (2019), arXiv:1903.04467 [gr-qc].

[42] R. Abbott *et al.* (LIGO Scientific Collaboration, Virgo Collaboration), Tests of general relativity with binary black holes from the second LIGO-Virgo gravitational-wave transient catalog, *Phys. Rev. D* **103**, 122002 (2021), arXiv:2010.14529 [gr-qc].

[43] R. Abbott *et al.* (LIGO Scientific, Virgo, KAGRA), Tests of General Relativity with GWTC-3, arXiv:2112.06861 [gr-qc] (2021).

[44] P. C. C. Freire, N. Wex, G. Esposito-Farese, J. P. W. Verbiest, M. Bailes, B. A. Jacoby, M. Kramer, I. H. Stairs, J. Antoniadis, and G. H. Janssen, The relativistic pulsar-white dwarf binary PSR J1738+0333 II. The most stringent test of scalar-tensor gravity, *Mon. Not. Roy. Astron. Soc.* **423**, 3328 (2012), arXiv:1205.1450 [astro-ph.GA].

[45] M. Kramer *et al.*, Strong-Field Gravity Tests with the Double Pulsar, *Phys. Rev. X* **11**, 041050 (2021), arXiv:2112.06795 [astro-ph.HE].

[46] R. Abuter *et al.* (GRAVITY), Detection of the gravitational redshift in the orbit of the star S2 near the Galactic centre massive black hole, *Astron. Astrophys.* **615**, L15 (2018), arXiv:1807.09409 [astro-ph.GA].

[47] T. Do *et al.*, Relativistic redshift of the star S0-2 orbiting the Galactic center supermassive black hole, *Science* **365**, 664 (2019), arXiv:1907.10731 [astro-ph.GA].

[48] K. Akiyama *et al.* (Event Horizon Telescope), First M87 Event Horizon Telescope Results. I. The Shadow of the Supermassive Black Hole, *Astrophys. J. Lett.* **875**, L1 (2019), arXiv:1906.11238 [astro-ph.GA].

[49] T. Clifton, P. G. Ferreira, A. Padilla, and C. Skordis, Modified Gravity and Cosmology, *Phys. Rep.* **513**, 1 (2012), arXiv:1106.2476 [astro-ph.CO].

[50] A. Einstein, Über Gravitationswellen, *Sitzungsber. Preuss. Akad. Wiss. Berlin (Math. Phys.)* **1918**, 154 (1918).

[51] F. Pretorius, Evolution of binary black hole spacetimes, *Phys. Rev. Lett.* **95**, 121101 (2005), arXiv:0507014 [gr-qc].

[52] M. Campanelli, C. O. Lousto, Y. Zlochower, B. Krishnan, and D. Merritt, Spin Flips and Precession in Black-Hole-Binary Mergers, *Phys. Rev. D* **75**, 064030 (2007), arXiv:gr-qc/0612076.

[53] J. G. Baker, J. Centrella, D.-I. Choi, M. Koppitz, and J. van Meter, Gravitational wave extraction from an inspiraling configuration of merging black holes, *Phys. Rev. Lett.* **96**, 111102 (2006), arXiv:gr-qc/0511103.

[54] C. V. Vishveshwara, Scattering of Gravitational Radiation by a Schwarzschild Black-hole, *Nature* **227**, 936 (1970).

[55] W. H. Press, Long Wave Trains of Gravitational Waves from a Vibrating Black Hole, *Astrophys. J.* **170**, L105 (1971).

[56] T. Regge, Stability of a Schwarzschild singularity, *Phys. Rev.* **108**, 1063 (1957).

[57] F. J. Zerilli, Effective potential for even parity Regge-Wheeler gravitational perturbation equations, *Phys. Rev. Lett.* **24**, 737 (1970).

[58] S. A. Teukolsky, Perturbations of a rotating black hole. 1. Fundamental equations for gravitational electromagnetic and neutrino field perturbations, *Astrophys. J.* **185**, 635 (1973).

[59] S. Chandrasekhar and S. L. Detweiler, The quasi-normal modes of the Schwarzschild black hole, *Proc. R. Soc. A* **344**, 441 (1975).

[60] S. L. Detweiler, Resonant oscillations of a rapidly rotating black hole, *Proc. Roy. Soc. Lond. A* **352**, 381 (1977).

[61] S. L. Detweiler, Black holes and gravitational waves. III. The resonant frequencies of rotating holes, *Astrophys. J.* **239**, 292 (1980).

[62] E. W. Leaver, *Proc. R. Soc. London Ser. A* **402**, 285 (1985).

[63] R. H. Price, Nonspherical perturbations of relativistic gravitational collapse. 1. Scalar and gravitational perturbations, *Phys. Rev. D* **5**, 2419 (1972).

[64] R. H. Price, Nonspherical Perturbations of Relativistic Gravitational Collapse. II. Integer-Spin, Zero-Rest-Mass Fields, *Phys. Rev. D* **5**, 2439 (1972).

[65] H.-P. Nollert, TOPICAL REVIEW: Quasinormal modes: the characteristic ‘sound’ of black holes and neutron stars, *Class. Quant. Grav.* **16**, R159 (1999).

[66] K. D. Kokkotas and B. G. Schmidt, Quasinormal modes of stars and black holes, *Living Rev. Rel.* **2**, 2 (1999), arXiv:gr-qc/9909058.

[67] O. Dreyer, B. J. Kelly, B. Krishnan, L. S. Finn, D. Garrison, and R. Lopez-Aleman, Black hole spectroscopy: Testing general relativity through gravitational wave observations, *Class. Quantum Grav.* **21**, 787 (2004), arXiv:gr-qc/0309007.

[68] E. Berti, V. Cardoso, and C. M. Will, On gravitational-wave spectroscopy of massive black holes with the space interferometer LISA, *Phys. Rev. D* **73**, 064030 (2006), arXiv:gr-qc/0512160.

[69] S. Gossan, J. Veitch, and B. S. Sathyaprakash, Bayesian model selection for testing the no-hair theorem with black hole ring-downs, *Phys. Rev. D* **85**, 124056 (2012), arXiv:1111.5819 [gr-qc].

qc].

[70] J. Meidam, M. Agathos, C. Van Den Broeck, J. Veitch, and B. S. Sathyaprakash, Testing the no-hair theorem with black hole ringdowns using TIGER, *Phys. Rev. D* **90**, 064009 (2014), arXiv:1406.3201 [gr-qc].

[71] E. Berti, V. Cardoso, G. Carullo, *et al.*, Black hole spectroscopy: from theory to experiment, arXiv:2505.23895 [gr-qc] (2025).

[72] R. Penrose, “Golden Oldie”: Gravitational Collapse: The Role of General Relativity, *Gen. Relativ. Gravit.* **34**, 1141 (2002).

[73] S. Klainerman, Mathematical Challenges of General Relativity, in *The Ninth Marcel Grossmann Meeting*, edited by V. G. Gurzadyan, R. T. Jantzen, and R. Ruffini (2002) pp. 28–43.

[74] P. T. Chruściel, J. Lopes Costa, and M. Heusler, Stationary Black Holes: Uniqueness and Beyond, *Living Rev. Relativity* **15**, 7 (2012), arXiv:1205.6112 [gr-qc].

[75] G. W. Gibbons, Vacuum Polarization and the Spontaneous Loss of Charge by Black Holes, *Commun. Math. Phys.* **44**, 245 (1975).

[76] R. D. Blandford and R. L. Znajek, Electromagnetic extractions of energy from Kerr black holes, *Mon. Not. R. Astron. Soc.* **179**, 433 (1977).

[77] R. S. Hanni, Limits on the charge of a collapsed object, *Phys. Rev. D* **25**, 2509 (1982).

[78] G. Carullo, D. Laghi, N. K. Johnson-McDaniel, W. Del Pozzo, O. J. C. Dias, M. Godazgar, and J. E. Santos, Constraints on Kerr-Newman black holes from merger-ringdown gravitational-wave observations, *Phys. Rev. D* **105**, 062009 (2022), arXiv:2109.13961 [gr-qc].

[79] G. Carullo, W. Del Pozzo, and J. Veitch, Observational Black Hole Spectroscopy: A time-domain multimode analysis of GW150914, *Phys. Rev. D* **99**, 123029 (2019), [Erratum: *Phys. Rev. D* **100**, 089903(E) (2019)], arXiv:1902.07527 [gr-qc].

[80] M. Isi, M. Giesler, W. M. Farr, M. A. Scheel, and S. A. Teukolsky, Testing the no-hair theorem with GW150914, *Phys. Rev. Lett.* **123**, 111102 (2019), arXiv:1905.00869 [gr-qc].

[81] C. D. Capano, M. Cabero, J. Westerweck, J. Abedi, S. Kastha, A. H. Nitz, A. B. Nielsen, and B. Krishnan, Observation of a multimode quasi-normal spectrum from a perturbed black hole, arXiv:2105.05238 [gr-qc] (2021).

[82] R. Cotesta, G. Carullo, E. Berti, and V. Cardoso, Analysis of Ringdown Overtones in GW150914, *Phys. Rev. Lett.* **129**, 111102 (2022), arXiv:2201.00822 [gr-qc].

[83] H. Siegel, M. Isi, and W. M. Farr, Ringdown of GW190521: Hints of multiple quasinormal modes with a precessional interpretation, *Phys. Rev. D* **108**, 064008 (2023), arXiv:2307.11975 [gr-qc].

[84] V. Gennari, G. Carullo, and W. Del Pozzo, Searching for ringdown higher modes with a numerical relativity-informed post-merger model, *Eur. Phys. J. C* **84**, 233 (2024), arXiv:2312.12515 [gr-qc].

[85] V. Varma, S. E. Field, M. A. Scheel, J. Blackman, D. Gerosa, L. C. Stein, L. E. Kidder, and H. P. Pfeiffer, Surrogate models for precessing binary black hole simulations with unequal masses, *Phys. Rev. Research* **1**, 033015 (2019), arXiv:1905.09300 [gr-qc].

[86] A. Gamboa *et al.*, Accurate waveforms for eccentric, aligned-spin binary black holes: The multipolar effective-one-body model seobnrv5ehm, *Phys. Rev. D* **112**, 044038 (2025), arXiv:2412.12823 [gr-qc].

[87] A. Nagar, R. Gamba, P. Rettegno, V. Fantini, and S. Bernuzzi, Effective-one-body waveform model for noncircularized, planar, coalescing black hole binaries: The importance of radiation reaction, *Phys. Rev. D* **110**, 084001 (2024), arXiv:2404.05288 [gr-qc].

[88] E. W. Leaver, Spectral decomposition of the perturbation response of the Schwarzschild geometry, *Phys. Rev. D* **34**, 384 (1986).

[89] N. Andersson, Evolving test fields in a black hole geometry, *Phys. Rev. D* **55**, 468 (1997), arXiv:gr-qc/9607064.

[90] H. Zhu *et al.*, Imprints of changing mass and spin on black hole ringdown, *Phys. Rev. D* **110**, 124028 (2024), arXiv:2404.12424 [gr-qc].

[91] A. Chavda, M. Lagos, and L. Hui, The impact of initial conditions on quasi-normal modes, (2024), arXiv:2412.03435 [gr-qc].

[92] M. De Amicis, E. Cannizzaro, G. Carullo, and L. Sberna, Dynamical quasinormal mode excitation, (2025), arXiv:2506.21668 [gr-qc].

[93] L. London, D. Shoemaker, and J. Healy, Modeling ringdown: Beyond the fundamental quasinormal modes, *Phys. Rev. D* **90**, 124032 (2014), [Erratum: *Phys. Rev. D* **94**, 069902 (2016)], arXiv:1404.3197 [gr-qc].

[94] K. Mitman *et al.*, Nonlinearities in Black Hole Ringdowns, *Phys. Rev. Lett.* **130**, 081402 (2023), arXiv:2208.07380 [gr-qc].

[95] M. H.-Y. Cheung *et al.*, Nonlinear Effects in Black Hole Ringdown, *Phys. Rev. Lett.* **130**, 081401 (2023), arXiv:2208.07374 [gr-qc].

[96] S. Ma and H. Yang, Excitation of quadratic quasinormal modes for Kerr black holes, *Phys. Rev. D* **109**, 104070 (2024), arXiv:2401.15516 [gr-qc].

[97] A. Buonanno, G. B. Cook, and F. Pretorius, Inspiral, merger and ring-down of equal-mass black-hole binaries, *Phys. Rev. D* **75**, 124018 (2007), arXiv:gr-qc/0610122.

[98] E. Berti *et al.*, Inspiral, merger and ringdown of unequal mass black hole binaries: A multipolar analysis, *Phys. Rev. D* **76**, 064034 (2007), arXiv:gr-qc/0703053.

[99] E. S. C. Ching, P. T. Leung, W. M. Suen, and K. Young, Wave propagation in gravitational systems: Late time behavior, *Phys. Rev. D* **52**, 2118 (1995), arXiv:gr-qc/9507035.

[100] S. Ma, M. A. Scheel, J. Moxon, K. C. Nelli, N. Deppe, L. E. Kidder, W. Throwe, and N. L. Vu, Merging black holes with Cauchy-characteristic matching: Computation of late-time tails, *Phys. Rev. D* **112**, 024003 (2025), arXiv:2412.06906 [gr-qc].

[101] M. De Amicis, S. Albanesi, and G. Carullo, Inspiral-inherited ringdown tails, *Phys. Rev. D* **110**, 104005 (2024), arXiv:2406.17018 [gr-qc].

[102] M. De Amicis *et al.*, Late-time tails in nonlinear evolutions of merging black holes, (2024), arXiv:2412.06887 [gr-qc].

[103] I. Kamaretsos, M. Hannam, and B. Sathyaprakash, Is black-hole ringdown a memory of its progenitor?, *Phys. Rev. Lett.* **109**, 141102 (2012), arXiv:1207.0399 [gr-qc].

[104] L. T. London, Modeling ringdown. II. Aligned-spin binary black holes, implications for data analysis and fundamental theory, *Phys. Rev. D* **102**, 084052 (2020), arXiv:1801.08208 [gr-qc].

[105] X. Jiménez Forteza, S. Bhagwat, P. Pani, and V. Ferrari, Spectroscopy of binary black hole ringdown using overtones and angular modes, *Phys. Rev. D* **102**, 044053 (2020), arXiv:2005.03260 [gr-qc].

[106] M. H.-Y. Cheung, E. Berti, V. Baibhav, and R. Cotesta, Extracting linear and nonlinear quasinormal modes from black hole merger simulations, *Phys. Rev. D* **109**, 044069 (2024), [Erratum: *Phys. Rev. D* **110**, 049902 (2024)], arXiv:2310.04489 [gr-qc].

[107] L. Magaña Zertuche *et al.*, High-Precision Ringdown Sur-

rogate Model for Non-Precessing Binary Black Holes, arXiv:2408.05300 [gr-qc] (2024).

[108] F. Nobili, S. Bhagwat, C. Pacilio, and D. Gerosa, Ringdown mode amplitudes of precessing binary black holes, arXiv:2504.17021 [gr-qc] (2025).

[109] M. Isi and W. M. Farr, Analyzing black-hole ringdowns, arXiv:2107.05609 [gr-qc] (2021).

[110] A. Dhani, Importance of mirror modes in binary black hole ringdown waveform, Phys. Rev. D **103**, 104048 (2021), arXiv:2010.08602 [gr-qc].

[111] X. Li, L. Sun, R. K. L. Lo, E. Payne, and Y. Chen, Angular emission patterns of remnant black holes, Phys. Rev. D **105**, 024016 (2022), arXiv:2110.03116 [gr-qc].

[112] G. Carullo, W. Del Pozzo, and J. Veitch, `pyRing`: a time-domain ringdown analysis python package, git.ligo.org/lscsoft/pyring (2023).

[113] G. Carullo *et al.*, Empirical tests of the black hole no-hair conjecture using gravitational-wave observations, Phys. Rev. D **98**, 104020 (2018), arXiv:1805.04760 [gr-qc].

[114] M. Giesler *et al.*, Overtones and nonlinearities in binary black hole ringdowns, Phys. Rev. D **111**, 084041 (2025), arXiv:2411.11269 [gr-qc].

[115] M. Isi, K. Chatzioannou, and W. M. Farr, Hierarchical test of general relativity with gravitational waves, Phys. Rev. Lett. **123**, 121101 (2019), arXiv:1904.08011 [gr-qc].

[116] S. Ma, K. Mitman, L. Sun, N. Deppe, F. Hébert, L. E. Kidder, J. Moxon, W. Throwe, N. L. Vu, and Y. Chen, Quasinormal-mode filters: A new approach to analyze the gravitational-wave ringdown of binary black-hole mergers, Phys. Rev. D **106**, 084036 (2022), arXiv:2207.10870 [gr-qc].

[117] S. Ma, L. Sun, and Y. Chen, Black Hole Spectroscopy by Mode Cleaning, Phys. Rev. Lett. **130**, 141401 (2023), arXiv:2301.06705 [gr-qc].

[118] S. Ma, L. Sun, and Y. Chen, Using rational filters to uncover the first ringdown overtone in GW150914, Phys. Rev. D **107**, 084010 (2023), arXiv:2301.06639 [gr-qc].

[119] N. Lu, S. Ma, O. J. Piccinni, L. Sun, and E. Finch, Statistical identification of ringdown modes with rational filters, (2025), arXiv:2505.18560 [gr-qc].

[120] R. Brito, A. Buonanno, and V. Raymond, Black-hole Spectroscopy by Making Full Use of Gravitational-Wave Modeling, Phys. Rev. D **98**, 084038 (2018), arXiv:1805.00293 [gr-qc].

[121] L. Pompili, E. Maggio, H. O. Silva, and A. Buonanno, Parametrized spin-precessing inspiral-merger-ringdown waveform model for tests of general relativity, Phys. Rev. D **111**, 124040 (2025), arXiv:2504.10130 [gr-qc].

[122] E. Maggio, H. O. Silva, A. Buonanno, and A. Ghosh, Tests of general relativity in the nonlinear regime: A parametrized plunge-merger-ringdown gravitational waveform model, Phys. Rev. D **108**, 024043 (2023), arXiv:2212.09655 [gr-qc].

[123] A. Ghosh, R. Brito, and A. Buonanno, Constraints on quasinormal-mode frequencies with LIGO-Virgo binary-black-hole observations, Phys. Rev. D **103**, 124041 (2021), arXiv:2104.01906 [gr-qc].

[124] A. Ramos-Buades, A. Buonanno, H. Estellés, M. Khalil, D. P. Mihaylov, S. Ossokine, L. Pompili, and M. Shiferaw, Next generation of accurate and efficient multipolar precessing-spin effective-one-body waveforms for binary black holes, Phys. Rev. D **108**, 124037 (2023), arXiv:2303.18046 [gr-qc].

[125] L. Pompili *et al.*, Laying the foundation of the effective-one-body waveform models SEOBNRv5: Improved accuracy and efficiency for spinning nonprecessing binary black holes, Phys. Rev. D **108**, 124035 (2023), arXiv:2303.18039 [gr-qc].

[126] X. Jiménez-Forteza, D. Keitel, S. Husa, M. Hannam, S. Khan, and M. Pürer, Hierarchical data-driven approach to fitting numerical relativity data for nonprecessing binary black holes with an application to final spin and radiated energy, Phys. Rev. D **95**, 064024 (2017), arXiv:1611.00332 [gr-qc].

[127] F. Hofmann, E. Barausse, and L. Rezzolla, The final spin from binary black holes in quasi-circular orbits, *Astrophys. J. Lett.* **825**, L19 (2016), arXiv:1605.01938 [gr-qc].

[128] J. G. Baker, W. D. Boggs, J. Centrella, B. J. Kelly, S. T. McWilliams, *et al.*, Mergers of non-spinning black-hole binaries: Gravitational radiation characteristics, Phys. Rev. D **78**, 044046 (2008), arXiv:0805.1428 [gr-qc].

[129] T. Damour and A. Nagar, A new analytic representation of the ringdown waveform of coalescing spinning black hole binaries, Phys. Rev. D **90**, 024054 (2014), arXiv:1406.0401 [gr-qc].

[130] L. Blanchet, Post-Newtonian theory for gravitational waves, *Living Rev. Relativity* **27**, 4 (2024), arXiv:1310.1528 [gr-qc].

[131] R. Cotesta, A. Buonanno, A. Bohé, A. Taracchini, I. Hinder, and S. Ossokine, Enriching the Symphony of Gravitational Waves from Binary Black Holes by Tuning Higher Harmonics, Phys. Rev. D **98**, 084028 (2018), arXiv:1803.10701 [gr-qc].

[132] C. Mills and S. Fairhurst, Measuring gravitational-wave higher-order multipoles, Phys. Rev. D **103**, 024042 (2021), arXiv:2007.04313 [gr-qc].

[133] H. Zhong, M. Isi, K. Chatzioannou, and W. M. Farr, Multidimensional hierarchical tests of general relativity with gravitational waves, Phys. Rev. D **110**, 044053 (2024), arXiv:2405.19556 [gr-qc].

[134] A. G. Abac *et al.*, GWTC-4.0: Tests of General Relativity, arXiv:2509.00000 [gr-qc] (2025).

[135] E. Payne, M. Isi, K. Chatzioannou, and W. M. Farr, Fortifying gravitational-wave tests of general relativity against astrophysical assumptions, Phys. Rev. D **108**, 124060 (2023), arXiv:2309.04528 [gr-qc].

[136] C. Pacilio, D. Gerosa, and S. Bhagwat, Catalog variance of testing general relativity with gravitational-wave data, Phys. Rev. D **109**, L081302 (2024), arXiv:2310.03811 [gr-qc].

[137] W. Del Pozzo and A. Nagar, Analytic family of post-merger template waveforms, Phys. Rev. D **95**, 124034 (2017), arXiv:1606.03952 [gr-qc].

[138] A. Nagar, G. Riemenschneider, G. Pratten, P. Rettegno, and F. Messina, Multipolar effective one body waveform model for spin-aligned black hole binaries, Phys. Rev. D **102**, 024077 (2020), arXiv:2001.09082 [gr-qc].

[139] N. Yunes, K. Yagi, and F. Pretorius, Theoretical Physics Implications of the Binary Black-Hole Mergers GW150914 and GW151226, Phys. Rev. D **94**, 084002 (2016), arXiv:1603.08955 [gr-qc].

[140] A. Maselli, P. Pani, L. Gualtieri, and E. Berti, Parametrized ringdown spin expansion coefficients: a data-analysis framework for black-hole spectroscopy with multiple events, Phys. Rev. D **101**, 024043 (2020), arXiv:1910.12893 [gr-qc].

[141] H. O. Silva, A. Ghosh, and A. Buonanno, Black-hole ringdown as a probe of higher-curvature gravity theories, Phys. Rev. D **107**, 044030 (2023), arXiv:2205.05132 [gr-qc].

[142] E. M. Sänger *et al.*, Tests of General Relativity with GW230529: a neutron star merging with a lower mass-gap compact object, arXiv:2406.03568 [gr-qc] (2024).

[143] A. K.-W. Chung and N. Yunes, Probing quadratic gravity with black-hole ringdown gravitational waves measured by LIGO-Virgo-KAGRA detectors, (2025), arXiv:2506.14695 [gr-qc].

[144] V. Cardoso, S. Hopper, C. F. B. Macedo, C. Palenzuela, and P. Pani, Gravitational-wave signatures of exotic compact ob-

jects and of quantum corrections at the horizon scale, *Phys. Rev. D* **94**, 084031 (2016), arXiv:1608.08637 [gr-qc].

[145] E. Maggio, L. Buoninfante, A. Mazumdar, and P. Pani, How does a dark compact object ringdown?, *Phys. Rev. D* **102**, 064053 (2020), arXiv:2006.14628 [gr-qc].

[146] S. Alexander and N. Yunes, Chern-Simons Modified General Relativity, *Phys. Rept.* **480**, 1 (2009), arXiv:0907.2562 [hep-th].

[147] A. K.-W. Chung, K. K.-H. Lam, and N. Yunes, Quasinormal mode frequencies and gravitational perturbations of spinning black holes in modified gravity through METRICS: The dynamical Chern-Simons gravity case, *Phys. Rev. D* **111**, 124052 (2025), arXiv:2503.11759 [gr-qc].

[148] L. Blanchet, Gravitational radiation from post-Newtonian sources and inspiralling compact binaries, *Living Rev. Rel.* **17**, 2 (2014), gr-qc/0202016.

[149] L. Blanchet and B. S. Sathyaprakash, Detecting the tail effect in gravitational wave experiments, *Phys. Rev. Lett.* **74**, 1067 (1995).

[150] L. Blanchet and B. S. Sathyaprakash, Signal analysis of gravitational wave tails, *Class. Quantum Grav.* **11**, 2807 (1994).

[151] K. G. Arun, B. R. Iyer, M. S. S. Qusailah, and B. S. Sathyaprakash, Probing the non-linear structure of general relativity with black hole binaries, *Phys. Rev. D* **74**, 024006 (2006), arXiv:gr-qc/0604067.

[152] N. Yunes and F. Pretorius, Fundamental Theoretical Bias in Gravitational Wave Astrophysics and the Parameterized Post-Einsteinian Framework, *Phys. Rev. D* **80**, 122003 (2009), arXiv:0909.3328 [gr-qc].

[153] C. K. Mishra, K. G. Arun, B. R. Iyer, and B. S. Sathyaprakash, Parametrized tests of post-Newtonian theory using Advanced LIGO and Einstein Telescope, *Phys. Rev. D* **82**, 064010 (2010), arXiv:1005.0304 [gr-qc].

[154] T. G. F. Li, W. Del Pozzo, S. Vitale, C. Van Den Broeck, M. Agathos, *et al.*, Towards a generic test of the strong field dynamics of general relativity using compact binary coalescence, *Phys. Rev. D* **85**, 082003 (2012), arXiv:1110.0530 [gr-qc].

[155] M. Agathos, W. Del Pozzo, T. G. F. Li, C. Van Den Broeck, J. Veitch, and S. Vitale, TIGER: A data analysis pipeline for testing the strong-field dynamics of general relativity with gravitational wave signals from coalescing compact binaries, *Phys. Rev. D* **89**, 082001 (2014), arXiv:1311.0420 [gr-qc].

[156] A. K. Mehta, A. Buonanno, R. Cotesta, A. Ghosh, N. Sennett, and J. Steinhoff, Tests of general relativity with gravitational-wave observations using a flexible theory-independent method, *Phys. Rev. D* **107**, 044020 (2023), arXiv:2203.13937 [gr-qc].

[157] M. Agathos, W. Del Pozzo, T. G. F. Li, C. Van Den Broeck, J. Veitch, and S. Vitale, TIGER: A data analysis pipeline for testing the strong-field dynamics of general relativity with gravitational wave signals from coalescing compact binaries, *Phys. Rev. D* **89**, 082001 (2014), arXiv:1311.0420 [gr-qc].

[158] J. Meidam *et al.*, Parametrized tests of the strong-field dynamics of general relativity using gravitational wave signals from coalescing binary black holes: Fast likelihood calculations and sensitivity of the method, *Phys. Rev. D* **97**, 044033 (2018), arXiv:1712.08772 [gr-qc].

[159] S. Roy, M. Haney, G. Pratten, P. T. H. Pang, and C. Van Den Broeck, An improved parametrized test of general relativity using the IMRPhenomX waveform family: Including higher harmonics and precession, (2025), arXiv:2504.21147 [gr-qc].

[160] G. Pratten *et al.*, Computationally efficient models for the dominant and subdominant harmonic modes of precessing binary black holes, *Phys. Rev. D* **103**, 104056 (2021), arXiv:2004.06503 [gr-qc].

[161] M. Colleoni, F. A. R. Vidal, C. García-Quirós, S. Akçay, and S. Bera, Fast frequency-domain gravitational waveforms for precessing binaries with a new twist, *Phys. Rev. D* **111**, 104019 (2025), arXiv:2412.16721 [gr-qc].

[162] A. Pai and K. G. Arun, Singular value decomposition in parametrised tests of post-Newtonian theory, *Class. Quantum Grav.* **30**, 025011 (2013), arXiv:1207.1943 [gr-qc].

[163] A. A. Shoom, P. K. Gupta, B. Krishnan, A. B. Nielsen, and C. D. Capano, Testing the post-Newtonian expansion with GW170817, *Gen. Rel. Grav.* **55**, 55 (2023), arXiv:2105.02191 [gr-qc].

[164] M. Saleem, S. Datta, K. G. Arun, and B. S. Sathyaprakash, Parametrized tests of post-Newtonian theory using principal component analysis, *Phys. Rev. D* **105**, 084062 (2022), arXiv:2110.10147 [gr-qc].

[165] P. Mahapatra *et al.*, Confronting General Relativity with Principal Component Analysis: Simulations and Results from GWTC-3 Events, (2025), arXiv:2508.06862 [gr-qc].

[166] S. A. Hughes and K. Menou, Golden binaries for LISA: Robust probes of strong-field gravity, *Astrophys. J.* **623**, 689 (2005), arXiv:astro-ph/0410148 [astro-ph].

[167] A. Ghosh *et al.*, Testing general relativity using golden black-hole binaries, *Phys. Rev. D* **94**, 021101(R) (2016), arXiv:1602.02453 [gr-qc].

[168] A. Ghosh, N. K. Johnson-McDaniel, A. Ghosh, C. K. Mishra, P. Ajith, W. Del Pozzo, C. P. L. Berry, A. B. Nielsen, and L. London, Testing general relativity using gravitational wave signals from the inspiral, merger and ringdown of binary black holes, *Class. Quantum Grav.* **35**, 014002 (2018), arXiv:1704.06784 [gr-qc].

[169] J. M. Bardeen, W. H. Press, and S. A. Teukolsky, Rotating black holes: Locally nonrotating frames, energy extraction, and scalar synchrotron radiation, *Astrophys. J.* **178**, 347 (1972).

[170] J. Healy and C. O. Lousto, Remnant of binary black-hole mergers: New simulations and peak luminosity studies, *Phys. Rev. D* **95**, 024037 (2017), arXiv:1610.09713 [gr-qc].

[171] X. Jiménez-Forteza, D. Keitel, S. Husa, M. Hannam, S. Khan, and M. Pürrer, Hierarchical data-driven approach to fitting numerical relativity data for nonprecessing binary black holes with an application to final spin and radiated energy, *Phys. Rev. D* **95**, 064024 (2017).

[172] S. W. Hawking, Gravitational radiation from colliding black holes, *Phys. Rev. Lett.* **26**, 1344 (1971).

[173] N. Cornish, L. Sampson, N. Yunes, and F. Pretorius, Gravitational Wave Tests of General Relativity with the Parameterized Post-Einsteinian Framework, *Phys. Rev. D* **84**, 062003 (2011), arXiv:1105.2088 [gr-qc].

[174] M. Vallisneri, Testing general relativity with gravitational waves: a reality check, *Phys. Rev. D* **86**, 082001 (2012), arXiv:1207.4759 [gr-qc].

[175] W. Jia *et al.* (members of the LIGO Scientific Collaboration), Squeezing the quantum noise of a gravitational-wave detector below the standard quantum limit, *Science* **385**, 1318 (2024), arXiv:2404.14569 [gr-qc].

[176] D. Ganapathy, V. Xu, W. Jia, C. Whittle, M. Tse, L. Bartotti, M. Evans, and L. McCuller, Probing squeezing for gravitational-wave detectors with an audio-band field, *Phys. Rev. D* **105**, 122005 (2022), arXiv:2203.03849 [astro-ph.IM].

[177] E. Capote *et al.*, Advanced LIGO detector performance in the fourth observing run, (2024), arXiv:2411.14607 [gr-qc].

[178] GWTC-4.0: Population Properties of Merging Compact Binaries, (2025), arXiv:2508.18083 [astro-ph.HE].

[179] B. P. Abbott *et al.* (LIGO Scientific, Virgo), Observation of Gravitational Waves from a Binary Black Hole Merger, *Phys. Rev. Lett.* **116**, 061102 (2016), arXiv:1602.03837 [gr-qc].

[180] B. P. Abbott *et al.* (KAGRA Collaboration, LIGO Scientific Collaboration, and Virgo Collaboration), Prospects for Observing and Localizing Gravitational-Wave Transients with Advanced LIGO, Advanced Virgo and KAGRA, *Living Rev. Relativity* **23**, 3 (2020), arXiv:1304.0670 [gr-qc].

[181] LIGO Scientific Collaboration, Virgo Collaboration, and KAGRA Collaboration, Gw250114 gwosc page (2025).

[182] LIGO Scientific Collaboration, Virgo Collaboration, and KAGRA Collaboration, Black hole spectroscopy and tests of general relativity with gw250114: Data release (2025).

[183] R. Kumar, C. Carroll, A. Hartikainen, and O. Martin, Arviz a unified library for exploratory analysis of bayesian models in python, *Journal of Open Source Software* **4**, 1143 (2019).

[184] D. Williams, J. Veitch, M. L. Chiofalo, P. Schmidt, R. P. Udall, A. Vajpeji, and C. Hoy, Asimov: A framework for coordinating parameter estimation workflows, *J. Open Source Softw.* **8**, 4170 (2023), arXiv:2207.01468 [gr-qc].

[185] T. P. Robitaille *et al.* (Astropy Collaboration), Astropy: A community Python package for astronomy, *Astron. and Astrophys.* **558**, A33 (2013), arXiv:1307.6212 [astro-ph.IM].

[186] A. M. Price-Whelan *et al.* (Astropy Collaboration), The Astropy Project: Building an Open-science Project and Status of the v2.0 Core Package, *The Astronomical Journal* **156**, 123 (2018), arXiv:1801.02634 [astro-ph.IM].

[187] A. M. Price-Whelan *et al.* (Astropy Collaboration), The Astropy Project: Sustaining and Growing a Community-oriented Open-source Project and the Latest Major Release (v5.0) of the Core Package, *Astrophys. J.* **935**, 167 (2022), arXiv:2206.14220 [astro-ph.IM].

[188] N. J. Cornish, T. B. Littenberg, B. Bécsy, K. Chatzioannou, J. A. Clark, S. Ghonge, and M. Millhouse, BayesWave analysis pipeline in the era of gravitational wave observations, *Phys. Rev. D* **103**, 044006 (2021), arXiv:2011.09494 [gr-qc].

[189] G. Ashton *et al.*, Bilby: A user-friendly Bayesian inference library for gravitational-wave astronomy, *Astrophys. J. Suppl. Ser.* **241**, 27 (2019), arXiv:1811.02042 [astro-ph.IM].

[190] I. M. Romero-Shaw *et al.*, Bayesian inference for compact binary coalescences with bilby: validation and application to the first LIGO–Virgo gravitational-wave transient catalogue, *Mon. Not. Roy. Astron. Soc.* **499**, 3295 (2020), arXiv:2006.00714 [astro-ph.IM].

[191] G. Ashton, C. Talbot, S. Roy, G. Pratten, T.-H. Pang, M. Agathos, T. Baka, E. Sänger, A. Mehta, J. Steinhoff, E. Maggio, A. Ghosh, A. Vijaykumar, R. Enficiaud, and L. Pompili, Bilby TGR (2025).

[192] W. Del Pozzo and J. Veitch, CPNest: an efficient python parallelizable nested sampling algorithm, <https://github.com/johnveitch/cpnest> (2025).

[193] J. S. Speagle, dynesty: a dynamic nested sampling package for estimating Bayesian posteriors and evidences, *Mon. Not. Roy. Astron. Soc.* **493**, 3132 (2020), arXiv:1904.02180 [astro-ph.IM].

[194] D. M. Macleod, J. S. Areeda, S. B. Coughlin, T. J. Massinger, and A. L. Urban, GWpy: A Python package for gravitational-wave astrophysics, *SoftwareX* **13**, 100657 (2021).

[195] D. Macleod, S. Coughlin, A. Southgate, D. Davis, M. Pitkin, J. Areeda, R. N. George, P. Altin, P. Godwin, L. Singer, *et al.*, gwpy/gwpy: Gwpy 3.0.9 (2024).

[196] A. Collette, *Python and HDF5* (O'Reilly, 2013).

[197] F. Perez and B. E. Granger, Ipython: A system for interactive scientific computing, *Computing in Science & Engineering* **9**, 21 (2007).

[198] T. Kluyver *et al.* (Jupyter Development Team), Jupyter Notebooks—a publishing format for reproducible computational workflows, in *IOS Press* (IOS Press, 2016) pp. 87–90.

[199] M. Beg, J. Taka, T. Kluyver, A. Konovalov, M. Ragan-Kelley, N. M. Thiéry, and H. Fangohr, Using jupyter for reproducible scientific workflows, *Computing in Science & Engineering* **23**, 36 (2021).

[200] LIGO Scientific Collaboration, Virgo Collaboration, and KAGRA Collaboration, LVK Algorithm Library - LALSuite, Free software (GPL) (2018).

[201] K. Wette, SWIGLAL: Python and Octave interfaces to the LALSuite gravitational-wave data analysis libraries, *SoftwareX* **12**, 100634 (2020), arXiv:2012.09552 [astro-ph.IM].

[202] T. A. Caswell, E. S. de Andrade, A. Lee, M. Droettboom, T. Hoffmann, J. Klymak, J. Hunter, E. Firing, D. Stansby, N. Varoquaux, *et al.*, matplotlib/matplotlib: Rel: v3.7.3 (2023).

[203] J. D. Hunter, Matplotlib: A 2d graphics environment, *Computing in Science & Engineering* **9**, 90 (2007).

[204] C. R. Harris, K. J. Millman, S. J. van der Walt, R. Gommers, P. Virtanen, D. Cournapeau, E. Wieser, J. Taylor, S. Berg, N. J. Smith, *et al.*, Array programming with NumPy, *Nature* **585**, 357 (2020).

[205] W. McKinney, Data Structures for Statistical Computing in Python, in *Proceedings of the 9th Python in Science Conference*, edited by Stéfan van der Walt and Jarrod Millman (2010) pp. 56 – 61.

[206] The pandas development team, pandas-dev/pandas: Pandas (2024).

[207] C. Hoy and V. Raymond, PESummary: the code agnostic Parameter Estimation Summary page builder, *SoftwareX* **15**, 100765 (2021), arXiv:2006.06639 [astro-ph.IM].

[208] D. P. Mihaylov, S. Ossokine, A. Buonanno, H. Estelles, L. Pompili, M. Pürer, and A. Ramos-Buades, pySEOBNR: a software package for the next generation of effective-one-body multipolar waveform models, *SoftwareX* **30**, 102080 (2025), arXiv:2303.18203 [gr-qc].

[209] G. Van Rossum and F. L. Drake, *Python 3 Reference Manual* (CreateSpace, Scotts Valley, CA, 2009).

[210] L. C. Stein, qnm: A Python package for calculating Kerr quasinormal modes, separation constants, and spherical-spheroidal mixing coefficients, *J. Open Source Softw.* **4**, 1683 (2019), arXiv:1908.10377 [gr-qc].

[211] M. Isi and W. M. Farr, RINGDOWN package, ringdown.readthedocs.io (2024).

[212] P. Virtanen *et al.* (SciPy 1.0 Contributors), SciPy 1.0: Fundamental Algorithms for Scientific Computing in Python, *Nature Methods* **17**, 261 (2020).

[213] R. Gommers, P. Virtanen, M. Haberland, E. Burovski, W. Weckesser, T. Reddy, T. E. Oliphant, D. Cournapeau, A. Nelson, *et al.*, scipy/scipy: Scipy 1.12.0 (2024).

[214] M. L. Waskom, seaborn: statistical data visualization, *Journal of Open Source Software* **6**, 3021 (2021).

[215] M. Khalil, A. Buonanno, H. Estelles, D. P. Mihaylov, S. Ossokine, L. Pompili, and A. Ramos-Buades, Theoretical groundwork supporting the precessing-spin two-body dynamics of the effective-one-body waveform models SEOBNRv5, *Phys. Rev. D* **108**, 124036 (2023), arXiv:2303.18143 [gr-qc].

[216] M. van de Meent, A. Buonanno, D. P. Mihaylov, S. Ossokine, L. Pompili, N. Warburton, A. Pound, B. Wardell, L. Durkan, and J. Miller, Enhancing the SEOBNRv5 effective-one-body

waveform model with second-order gravitational self-force fluxes, *Phys. Rev. D* **108**, 124038 (2023), arXiv:2303.18026 [gr-qc].

[217] M. Boyle, K. Mitman, M. Scheel, and L. Stein, The SXS package (2025).

[218] C. da Costa-Luis, S. K. Laroque, K. Altendorf, H. Mary, R. Sheridan, M. Korobov, N. Yorav-Raphael, I. Ivanov, M. Bargull, N. Rodrigues, *et al.*, tqdm: A fast, extensible progress bar for Python and CLI (2024).

[219] C. Talbot *et al.*, Inference with finite time series II: the window strikes back, (2025), arXiv:2508.11091 [gr-qc].

[220] A. G. Abac *et al.* (LIGO Scientific, VIRGO, KAGRA), GWTC-4.0: Methods for Identifying and Characterizing Gravitational-wave Transients, (2025), arXiv:2508.18081 [gr-qc].

[221] V. Baibhav, M. H.-Y. Cheung, E. Berti, V. Cardoso, G. Carullo, R. Cotesta, W. Del Pozzo, and F. Duque, Agnostic black hole spectroscopy: Quasinormal mode content of numerical relativity waveforms and limits of validity of linear perturbation theory, *Phys. Rev. D* **108**, 104020 (2023), arXiv:2302.03050 [gr-qc].

[222] K. Mitman *et al.*, Probing the ringdown perturbation in binary black hole coalescences with an improved quasi-normal mode extraction algorithm, arXiv:2503.09678 [gr-qc] (2025).

[223] SXS Collaboration, SXS Gravitational Waveform Database, <http://www.black-holes.org/waveforms/>.

[224] M. A. Scheel *et al.*, The SXS Collaboration’s third catalog of binary black hole simulations, (2025), arXiv:2505.13378 [gr-qc].

[225] G. B. Cook, Aspects of multimode Kerr ringdown fitting, *Phys. Rev. D* **102**, 024027 (2020), arXiv:2004.08347 [gr-qc].

[226] R. D. Morey, J.-W. Romeijn, and J. N. Rouder, The philosophy of bayes’ factors and the quantification of statistical evidence, *Journal of Mathematical Psychology* **72**, 6 (2016).

[227] J. M. Dickey, The Weighted Likelihood Ratio, Linear Hypotheses on Normal Location Parameters, *Ann. Math. Statist.* **42**, 204 (1971).

[228] A. Zimmerman, C.-J. Haster, and K. Chatzioannou, On combining information from multiple gravitational wave sources, *Phys. Rev. D* **99**, 124044 (2019), arXiv:1903.11008 [astro-ph.IM].

[229] A. Akyüz, A. Correia, J. Garofalo, K. Kacanja, L. Roy, K. Soni, H. Tan, V. J. Y. A. H. Nitz, and C. D. Capano, Potential science with GW250114 – the loudest binary black hole merger detected to date, arXiv eprints (2025), arXiv:2507.08789 [gr-qc].

[230] C. Xin, M. Isi, W. M. Farr, and Z. Haiman, Identifying Compact Chirping SMBHBs in LSST using Bayesian Analysis, arXiv eprints (2025), arXiv:2506.10846 [astro-ph.HE].